Biochemistry

pubs.acs.org/biochemistry
Article

Characterization of Regioisomeric Conjugates Arising from Pixantrone at AP Sites in DNA

Yizhi Fu, John T. Terrell, Andrew Kellum, Pradeep S. Pallan, Rodrigo Galindo-Murillo, Carmelo J. Rizzo, Martin Egli, and Michael P. Stone*

Cite This: https://doi.org/10.1021/acs.biochem.6c00116
Read Online

ABSTRACT: Alkylation at N7 of guanine leads to formation of abasic (AP) sites in DNA. These equilibrate between α and β anomers and form conjugates with 6,9-bis[(2-aminoethyl)amino]-benzo[g]isoquinoline-5,10-dione (Pixantrone, PIX). NMR revealed that these conjugates formed as regioisomeric Schiff base products R_a and R_b arising from the nonequivalent PIX C6 and C9 2-aminoethyl side chains. In dsDNA formation of R_a was favored. In ssDNA, both products formed equally. Structures of reduced R_a and R_b conjugates from molecular dynamics calculations restrained by ^{1}H NOESY data in 5′-d(C^{1}A^{2}G^{3}A^{4}C^{5}T^{6}X^{7}A^{8}G^{9}A^{10}C^{11}T^{12})-3′:5′-d(A^{13}G^{14}T^{15}C^{16}T^{17}C^{18}A^{19}G^{20}T^{21}C^{22}T^{23}G^{24})-3′, X = reduced PIX-AP site conjugate, showed that both regioisomers intercalated on the 3′ side of base pair T^6/A^{19}, displacing C^{18} into the major groove, with R_a less intercalated than R_b. The preferential formation of R_a vs R_b in dsDNA and deeper intercalation of R_b may be explained by the differential ability of the asymmetric PIX N2 nitrogen in R_a vs R_b to hydrogen bond with the exocyclic N^4-amine of the cytosine displaced into the major groove. MD simulations in dsDNA with R_a and R_b reduced PIX AP site conjugates revealed that for both, the isoquinoline first reoriented within the minor groove. The complementary cytosine rotated toward the major groove, allowing intercalation of the R_a and R_b conjugates. Binding energy analyses yielded values of −108.1 (±9.7) kcal/mol and −102.2 (±8.3) kcal/mol for the intercalated R_a and R_b conjugates, respectively. A crystal structure in the Dickerson-Drew Dodecamer at 2.5 Å resolution revealed looped-out PIX stacking with PIX from a neighboring duplex.

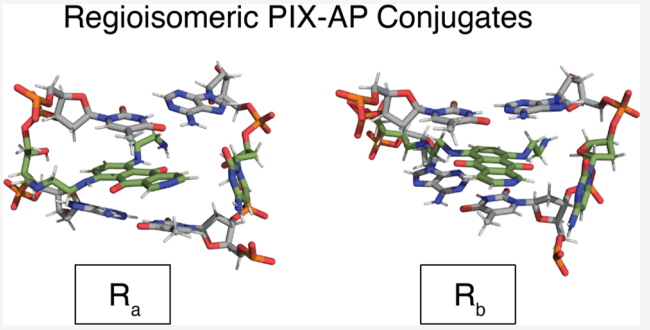

INTRODUCTION

Abasic sites (AP sites) result from spontaneous depurination of canonical and chemically modified nucleobases in DNA[1−3] but also from DNA alkylation during chemotherapy.[3,4] They also form during the removal of damaged nucleobases by base excision repair (BER).[5] Spontaneous depurination generates ∼10^4 AP sites per cell per day, which are removed by AP endonucleases, with steady-state levels of one AP site per 10^7 nt.[4,6,7] Structurally, AP sites retain a B-DNA conformation.[8,9] However, they are genotoxic, with different dNTPs incorporated opposite these lesions depending on the polymerase and DNA sequence context.[10,11] AP sites equilibrate between α and β anomers of the 2′-deoxyribosyl sugar via a ring-opened aldehyde,[8,9,12−14] which places transient levels of an electrophilic aldehyde into the DNA. This renders AP sites in DNA reactive to both endogenous and exogenous amines;[3] consequently, they form interstrand DNA cross-links,[14−16] as well as DNA−protein conjugates.[17,18] Covalent DNA−protein cross-links (DPCs) with repair-associated proteins such as 5-hydroxymethylcytosine binding, embryonic stem-cell-specific (HMCES)[19] protect the genome by shielding AP sites from endonuclease cleavage and replication-associated processing arising from DNA damage or replication stress.[20] Bellamri et al.[21] demonstrated that amino groups of the antitumor agents doxorubicin (DOX), mitoxantrone (MTX), and pixantrone (PIX) (Chart 1) may react with AP sites to form Schiff base conjugates.

Pixantrone (PIX), 6,9-bis[(2-aminoethyl)amino]benzo[g]-isoquinoline-5,10-dione (CAS Registry 144510-96-3), is a cytotoxic, synthetic aza-anthracenedione antitumor agent.[22] Its cytotoxicity is believed to involve intercalation into DNA and interference with DNA-topoisomerase II activity during cell division, leading to protein-associated DNA strand breaks and cell death. PIX is a noncardiotoxic[22] structural analog of MTX, 1,4-dihydroxy-5,8-bis[2-(2-hydroxyethylamino)ethylamino]-anthracene-9,10-dione.[23,24] The aza-anthracenedione ring of PIX is believed to reduce cardiotoxicity by a combination of

Received: April 10, 2026
Revised: June 24, 2026
Accepted: July 3, 2026

Chart 1. (A) Structures of regioisomeric PIX-AP conjugates, R_a (left) and R_b (right). (B) Oligodeoxynucleotide used in this work, showing numbering of individual nucleotides. (C) Structures of mitoxantrone (MTX) and doxorubicin (DOX)

A

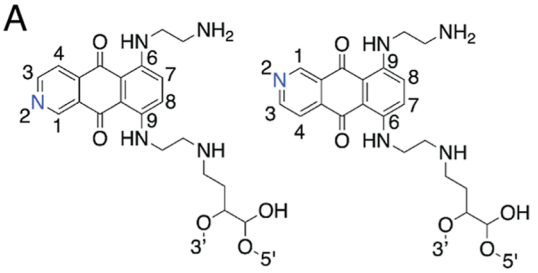

B

$5'\text{-d}(C^1\,A^2\,G^3\,A^4\,C^5\,T^6\,X^7\,A^8\,G^9\,A^{10}C^{11}T^{12})\text{-}3'$
$3'\text{-d}(G^{24}T^{23}C^{22}T^{21}G^{20}A^{19}C^{18}T^{17}C^{16}T^{15}G^{14}A^{13})\text{-}5'$

C

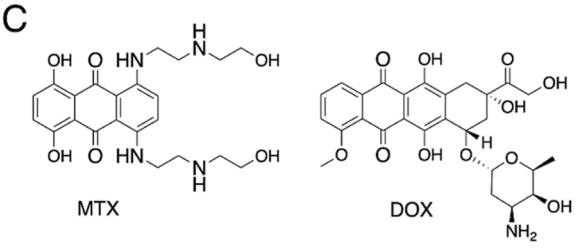

factors, including its reduced redox cycling ability, reduced ability to bind Fe(III), and its selectivity for topoisomerase IIa in stabilizing topoisomerase-DNA covalent complexes, as opposed to topoisomerase IIb, expressed in cardiac tissue.[25] The nitrogen atom in the PIX aza-anthracenedione ring renders the two side-chain amines nonequivalent, and predicts the formation of regioisomeric Schiff base conjugates with AP sites in DNA, referred to as regioisomers A and B and designated as R_a and R_b (Chart 1).

Here, we investigate PIX conjugation at AP sites in DNA. We prepared reduced analogs of site-specific PIX-AP site conjugates in oligodeoxynucleotides (Chart 1). We show that PIX forms regioisomeric Schiff base conjugates with AP sites. We identify and characterize these reduced PIX-AP site conjugates using NMR spectroscopy, showing that the regioisomers form equally in ssDNA but at differential levels in dsDNA. We employed restrained molecular dynamics (rMD) simulations to determine structures for the two regioisomers. Both intercalate, displacing the complementary cytosine into the major groove. Calculations and thermal melting studies reveal that both have similar energies. Unbiased molecular dynamics (MD) simulations indicate that PIX intercalates at AP sites from the DNA minor groove, shifting the nonpaired nucleotide in the complementary strand toward the major groove. A possible explanation for the differential distribution of regioisomers is that the reaction proceeds under kinetic control, modulated by differences in pixantrone intercalation geometries involving the nitrogen atom in the PIX aza-anthracenedione ring. Formation of the less favored regioisomer might involve a transient H-bonding interaction between the ligand and the exocyclic amino group of the opposing cytosine, which could hinder Schiff-base formation at the AP site. We also present a crystal structure of PIX-AP conjugates in the Dickerson-Drew Dodecamer (DDD, 5′-d(CGCXAATTCGCG)-3′, X = PIX-AP) refined to a resolution of 2.5 Å. The structure revealed disruption of the DNA duplex and an extrahelical PIX engaged in a stacking interaction with a second extrahelical PIX from a neighboring DNA duplex.

MATERIALS AND METHODS

Unbiased Molecular Dynamics Simulations

The Dickerson-Drew DNA (DDD) dodecamer duplex [5′-d(CGCGAATTCGCG)-3′]$_2$ was constructed using DS Visualizer,[26] DNA nucleotides in the two strands were numbered 1 to 12 and 13 to 24. PIX was constructed using GaussView 6[27] and optimized using Gaussian 16 (M02-2x/6-31G*).[28] The DDD was described with the OL15 AMBER force field[29] and PIX was described by the General Amber Force Field[30] with charges obtained with the RESP[31] fitting scheme. The systems were solvated using the optimum point charge water model[32] within a truncated octahedral periodic cell with a 10 Å buffer. Na^+ and Cl^- ions were added to neutralize the charge and additional ions to reach a final concentration of 200 mM using the Joung−Cheatham parameters.[33] Topologies were created using the tleap module of AmberTools 21.[34] Initial relaxation, heating and minimization was performed using the 9-step protocol implemented in the AmberMD tool.[35] Simulations were calculated using the GPU version of pmemd[36] at 310 K with a Monte Carlo barostat, within the NTP ensemble. Temperature was regulated using Langevin dynamics (gamma = 0.01). All simulations were computed using three independent replicas, each ∼5 μs. Analysis was performed using CPPTRAJ version V6.15.0.[37,38]

Oligodeoxynucleotide Synthesis and Purification

The dodecamer 5′-d(CAGACTUAGACT)-3′, containing a site-specific uracil nucleotide, was obtained commercially (Integrated DNA Technologies; Coralville, Iowa). *Escherichia coli* uracil-DNA glycosylase[5] (UDG; EC 3.2.2.3; New England Biolabs; Ipswich, MA) (0.25 units/μL) was added to the uracil-containing dodecamer in 10 mM NaCl, 100 mM 4-(2-hydroxyethyl)-1-piperazineethanesulfonic acid (HEPES; pH 7.4) with total volume of 1 mL for 1.5 h at 37 °C. Pixantrone dimaleate (Biosynth; Staad, Switzerland) (100 μM) was added simultaneously with sodium cyanoborohydride (Na-[BH_3(CN)]) (50 mM). Pixantrone is cytotoxic. Sodium cyanoborohydride is toxic. Both should be handled in a fume hood with appropriate personal protective equipment. The mixture was incubated for 3 h at 37 °C; the dodecamer 5′-dCAGACTXA-GACT-3′, X = reduced PIX-AP site conjugate, was purified by reverse-phase HPLC, with a Gemini C_{18} column (4.6 mm internal diameter, 10 mm particle size) at flow rate of 1.5 mL/min. The mobile phase was derived by mixing solvent A, 0.1 M ammonium formate (pH 7), with solvent B, acetonitrile. The gradient was 1% to 10% solvent B over 15 min, followed by 10% to 20% solvent B over 5 min, held isocratic for 5 min, then increased to 80% solvent B over 2 min, held isocratic at 80% solvent B for 3 min, then decreased to 0% solvent B over 2 min. The purified dodecamer containing the reduced PIX-AP site conjugate was lyophilized, dissolved in 1 mL of H_2O, and annealed with the complementary dodecamer 5′-d(AGTCTCAGTCTG)-3′. The duplex dodecamer containing the reduced PIX-AP site conjugate was passed over a hydroxyapatite (HAP) column (Econo-Column, 2.5 × 10 cm, Bio-Rad, Inc., Hercules, CA), equilibrated with 200 mM NaH_2PO_4 (pH 7). Buffer A contained 100 mM NaCl, 50 μM disodium ethylenediaminetetraacetic acid (Na_2EDTA), and 10 mM NaH_2PO_4 (pH 7); buffer B contained 100 mM NaCl, 50 μM Na_2EDTA, and 200 mM NaH_2PO_4. (pH 7). A linear gradient from 0% to 25% Buffer B was run for 1 h, followed by a linear gradient from 25% to 100% buffer B for 40 min, and the HAP column was maintained at 100% B for 20 min. The dodecamer duplex was desalted by passing through Sephadex G-25 (Sigma-Aldrich, St. Louis, MO) packed into a chromatography

https://doi.org/10.1021/acs.biochem.6c00116
Biochemistry XXXX, XXX, XXX−XXX

column (Econo-Column, 1.5 × 75 cm, Bio-Rad Inc., Hercules, CA). Desalting was carried out at a flow rate of 2.0 mL/min using deionized water. DNA elution was monitored by UV absorbance at 260 nm and salt elution was monitored by conductivity.

For crystallographic studies, an aliquot of UDG was added to a solution containing 50 μM 5′-d(CGCUAATTCGCG)-3′ in 100 mM KCl and 20 μM Tris−HCl (pH 7.4). The solution was incubated at room temperature for 1 h. Next, a 2-fold molar excess of pixantrone dimaleate (Biosynth Carbosynth) was added. Subsequently, an excess of freshly prepared sodium cyanoborohydride was added and the solution incubated at room temperature for 3 h. The resulting PIX-conjugated DDD 5′-CGCXAATTCGCG-3′ was then purified by reverse phase HPLC.

Mass Spectrometry

Mass-to-charge ratios (m/z) of oligodeoxynucleotides were measured using a ultraflexXtreme MALDI-TOF/TDF mass spectrometer (Bruker Instruments, Inc., Billerica, MA). Samples were prepared by mixing 10 μL of 0.5 M of 3-hydroxypicolinic acid (HPA), 5 μL of 0.1 M ammonium hydrogen citrate (AHC), and 2 μL of DNA. Both HPA and AHC solutions were dissolved in 1:1 (v/v) acetonitrile/water solution. Mass spectra were acquired in negative ion mode.

PIX Conjugation Studies

PIX was incubated for 0.5, 1, and 3 h with the duplex dodecamer 5′-d(CAGACTUAGACT)-3′:5′-d(AGTCTCAGTCTG)-3′, containing a site-specific uracil nucleotide, in 1 mM NaCl, 100 mM HEPES (pH 7.4) with total volume of 1 mL, as a function of temperature. For single strand DNA studies, pixantrone was incubated with the dodecamer 5′-d(CAGACTUAGACT)-3′, containing a site-specific uracil nucleotide, for 0.5, 1, and 3 h in 1 mM NaCl, 100 mM HEPES (pH 7.4) with total volume of 1 mL, as a function of temperature. For both duplex DNA and single-strand DNA studies, pixantrone (100 μM) was added simultaneously with Na[BH_3(CN)] (50 mM). In dsDNA, reactions were monitored at 0 °C, 25 °C, 35 °C, and 60 °C. In ssDNA, reactions were monitored at 0 °C, 37 and 60 °C. At 0.5, 1, and 3 h, reactions were quenched using 1 M methoxyamine (MX).[39] The regioisomeric distributions of reduced AP site conjugates were analyzed by ^{1}H NMR by integrating the pixantrone H1 and H3 proton signals (Chart 1).

Melting Temperature (T_m) Experiments

The absorbances of 5 μM 5′-d(CAGACTXAGACT)-3′:5′-d-(AGTCTCAGTCTG)-3′ (X = reduced PIX-AP site conjugate, or tetrahydrofuran (THF)), and of the corresponding unmodified duplex were measured in 1 M NaCl, 50 μM Na_2EDTA, and 10 mM NaH_2PO_4 (pH 7), at 260 nm, using a 1 cm path length cuvette. Thermal scans were performed from 5 to 85 °C in 1 °C/min intervals. Melting temperature (T_m) values were determined from first derivative analyses of plots obtained for DNA absorbance at 260 nm as a function of temperature. All experiments were performed on a Cary 100 Bio UV/vis spectrometer equipped with a Peltier thermal cycler (Agilent, Santa Clara, CA, USA).

NMR Spectroscopy

The 5′-d(CAGACTXAGACT)-3′:5′-d(AGTCTCAGTCTG)-3′ (X = reduced PIX-AP site conjugate) and the unmodified duplex 5′-d(CAGACTGAGACT)-3′:5′-d(AGTCTCAGTCTG)-3′ were prepared in 100 mM NaCl, 50 μM Na_2EDTA, and 10 mM NaH_2PO_4 (pH 7.0). The concentrations of dodecamer duplexes were 300 μM. The sample volumes were maintained at 250 μL. Data were collected in 5 mm NMR tubes with cryogenic probes (Bruker Biospin, Inc., Billerica, MA). ^{1}H COSY[40] spectra and NOESY[41,42] spectra of nonexchangeable protons were obtained in buffer containing 99.996% D_2O at 288 K, while NOESY spectra of exchangeable protons were obtained in buffer containing 95:5 H_2O/D_2O at 274 K. NOESY spectra of nonexchangeable protons were collected at 100 ms and 250 ms mixing times, and a relaxation delay of 1.5 s. Spectra were acquired with 2048 complex points in the direct dimension (t_2) and 512 increments in the indirect dimension (t_1). The t_1 dimension was zero-filled to 2048 points, resulting in a final processed matrix of 2048 × 2048 data points. Data were analyzed using TOPSPIN (Bruker Biospin, Billerica, MA, USA) and processed using SPARKY.[43]

NMR Distance Restraints

The volumes of NOESY cross-peaks were integrated from spectra recorded with mixing time of 250 ms at 288 K. The intrinsic integration error was estimated as half of the volume of the weakest cross-peak. Cross-peaks were assigned error values across five levels based on their characteristics. Well-resolved and nonoverlapping cross-peaks were assigned a 10% error margin. A 20% error was applied to strong, slightly broadened, or moderately overlapped cross-peaks with medium signal-to-noise ratios (S/N). Cross-peaks that were strong but moderately broadened or overlapped were assigned a 30% error. A 40% error was attributed to peaks with weak S/N or slight overlap. Highly broadened cross-peaks near the diagonal or water suppression, or those with moderate S/N and overlap, were assigned a 50% error.[44−46] Distance restraints were generated using MARDIGRAS.[47] Additional restraints were applied based on canonical Watson−Crick H-bonding distances for B-DNA base pairs.[48] Watson−Crick H-bonding restraints were not employed for the T^6/A^{19} base pair and for the C^{18} base opposite X^7. Restraints for deoxyribose pseudorotation and phosphodiester backbone torsion angles were based on canonical B-DNA values.[48] Backbone torsion angles were assigned potential energy wells with a window of ±30°, except for nucleotides T^6, X^7, C^{18}, and A^{19}, which were assigned wider windows of ±60°. Backbone torsion angle restraints were centered on typical B-DNA torsion values: $\alpha = -60°$, $\beta = 180°$, $\gamma = 60°$, $\varepsilon = 195°$, and $\zeta = -105°$. Partial charges and bond lengths for regioisomeric PIX-AP conjugates were determined using GAUSSIAN with the B3LYP/6-31G* basis set.[28]

Restrained Molecular Dynamics Simulations

Starting structures of the regioisomeric reduced PIX-AP site conjugates were constructed using MOE,[49] where the unmodified duplex containing G^7 was first generated and subsequently modified to the reduced PIX-AP site conjugate using the Builder tool in AMBER.[34] Further processing was performed in xLEAP,[50,51] where partial charges and bond lengths for reduced PIX-AP site conjugates obtained from GAUSSIAN[28] were incorporated. Parameter and coordinate files (.top and.inp) were generated using the AMBER suite of programs.[34,52] Restrained molecular dynamics (rMD) calculations were performed using a simulated annealing protocol implemented in AMBER[34] with the parm99 force field.[53] Solvation was modeled using the generalized Born model,[54] with the salt concentration set at 0.1 M. A force constant of 30 kcal mol^{-1} Å^{-2} was applied to all restraints. Initial calculations were carried out over 100 ps for 100,000 steps. The system was heated from 0 to 600 K during the first 3000 steps using a 0.5 ps coupling constant and maintained at 600 K for the remaining steps. NOE-derived distance restraints were compared to calculated intensities from emergent structures using complete relaxation matrix analysis with CORMA.[47] The 20 structures with the lowest deviations from experimental distance restraints were averaged to generate a refined structure. Structural renderings were created using CHIMERA.[55]

Crystal Growth

Crystallization trials were performed with the Crystal Screen 1[56] Crystal Screen 2, Natrix 1, Natrix 2, and Nucleic Acid Mini Screen[57] (Hampton Research, Aliso Viejo, CA). DNA was desalted and prepared at a concentration of 1 mM in DNase- and RNase-free water. The hanging drop vapor diffusion technique was used. Droplets with volumes of 2 μL and composed of a 1:1 mixture of sample and crystallization solution were equilibrated against a 600 μL well solution. A slightly modified condition that resulted in crystals of the native oligonucleotide was used to grow crystals of the dodecamer containing 5Br−C:5′-d(CGCXAATT(5-BrC)GCG)-3′. It consisted of 2.2 M ammonium sulfate, and 2.8% to 3.8% PEG400, in 0.1 M HEPES sodium (pH 7.5). Purple crystals grew within 1 wk.

https://doi.org/10.1021/acs.biochem.6c00116
Biochemistry XXXX, XXX, XXX−XXX

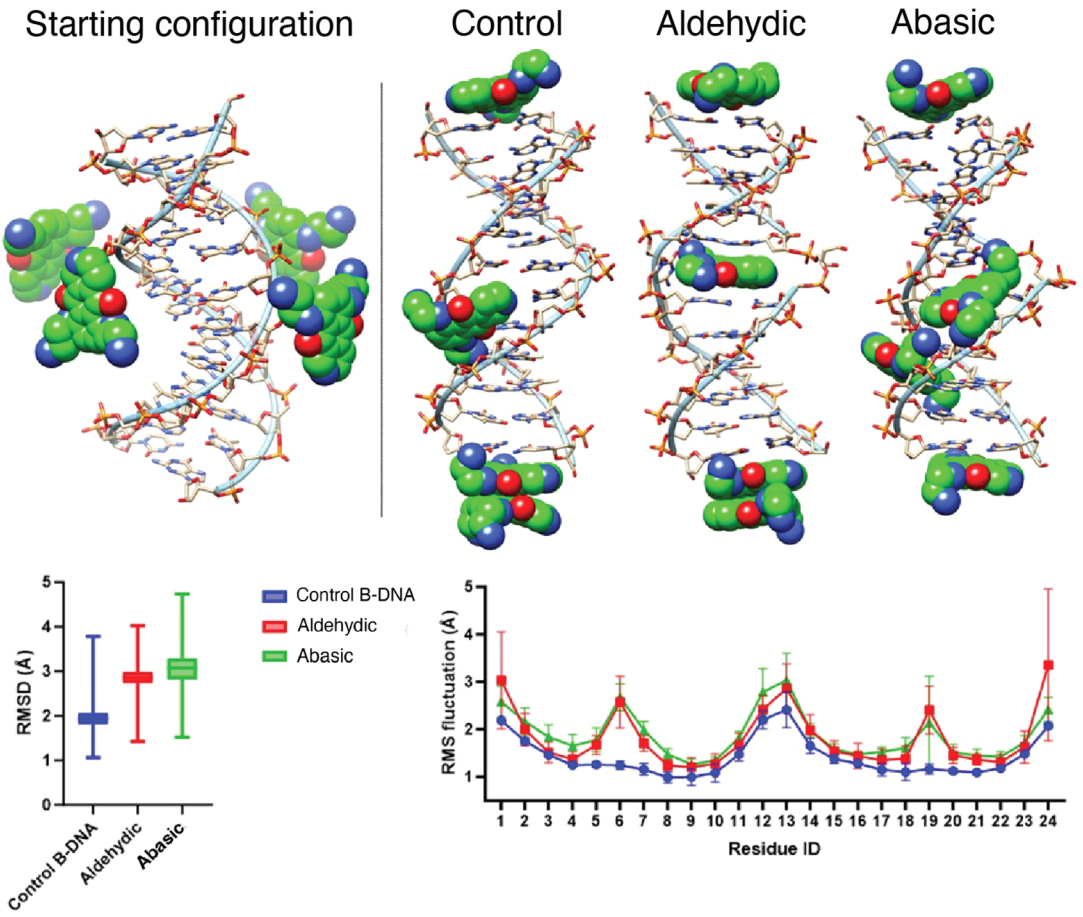

Figure 1. Top left -starting conformation of all the MD simulations. Top-right—representative structures of most populated clusters using five independent replicate. RMSD values calculated using the first frame as reference (showing SD). RMS fluctuations and RMSD values calculated using five independent replicate. Pixantrone carbon atoms are in green.

Diffraction Data Collection, Phasing and Refinement

Crystals were cryoprotected in a solution consisting of the crystallization condition supplemented with 25% glycerol, mounted in a nylon loop, and frozen in liquid nitrogen. Diffraction data were collected in a cold nitrogen stream on beamline 21-ID-D at LS-CAT, APS (Argonne National Laboratory, Argonne, IL, USA) using a wavelength of 0.9184 Å. Reflections were integrated, scaled, and merged using the program HKL2000.[58] The structure was phased by Br-SAD using Phenix Autosol[59−61] and the asymmetric unit of the crystal in space group $P6_422$ contains two DNA strands. The experimental map after density modification was used to build 22 of the 24 residues with the program COOT.[62] The initial model was refined in Refmac 5[63] keeping aside 7% of the reflections to compute R-free.[64] After three cycles of refinement, 5Br−C and PIX residues were built into the electron density, and refinement was continued in Refmac 5 using a dictionary generated using PRODRG.[65] Water molecules and several ethylene glycol molecules were added into overlapping positive peaks of Fourier 2Fo-Fc sum and Fo-Fc difference electron densities and accepted on the basis of standard distance criteria. Coordinates and structure factors for the final PIX-DNA model were deposited in the Protein Data Bank (http://www.rcsb.org): PDB ID 7U38.

RESULTS

Unbiased PIX-DNA MD Simulations

Unbiased MD simulations were performed to probe PIX binding to the Dickerson-Drew dodecamer (DDD). The starting structure was constructed by adding four PIX molecules at 10 Å of the DDD. Three systems were tested: DNA with an AP site (furanose with no base present), an aldehydic form, and unmodified DNA (control). For each, the representative structure of the most populated cluster is shown in Figure 1. The unmodified dsDNA showed PIX interacting within the minor groove and short-lived preintercalation events, where the PIX aromatic component pushed the paired bases toward the major groove. The simulation in which the dsDNA featured the ring-open aldehydic AP site presented events of the PIX intercalated into the gap that was formed when the unpaired cytosine flipped toward the major groove. Simulations having the AP site in dsDNA showed similar interactions as those seen between DNA and PIX, with PIX interacting from the minor groove. It is possible that with extended sampling time, the AP site would show increased intercalation events missing at this time scale. The structural deviation (RMSD) values of the models showed that the three systems were within ∼2−4 Å to the initial (reference) structure. The per nucleotide fluctuations showed increased values of nucleotides within the AP and aldehydic site that were not observed in the control. Small molecules, especially molecules with aromatic regions, tend to form stacking interactions with the terminal base pairs of short nucleic acid duplexes, which was observed here.

NMR Analysis

The duplex 5′-d($C^1A^2G^3A^4C^5T^6\underline{X}^7A^8G^9A^{10}C^{11}T^{12}$)-3′:5′-d-($A^{13}G^{14}T^{15}C^{16}T^{17}C^{18}A^{19}G^{20}T^{21}C^{22}T^{23}G^{24}$)-3′ ($\underline{X}$ = reduced PIX-AP site conjugate), was analyzed by ^{1}H NMR. Spectra

https://doi.org/10.1021/acs.biochem.6c00116
Biochemistry XXXX, XXX, XXX−XXX

were recorded over a temperature range of 278 to 308 K. This temperature range was below the T_m of the duplex, ensuring sharp NMR signals for the duplex DNA. The optimal temperature for collecting nonexchangeable ^{1}H data was 288 K, while spectra of Watson−Crick hydrogen-bonded imino- and amino exchangeable protons were best collected at 274 K to minimize exchange broadening.

Nonexchangeable DNA Protons. The sequential ^{1}H NMR assignments of the unmodified and the modified duplexes were completed using standard protocols (Figure 2).[66,67] For the modified strand 5′-d-

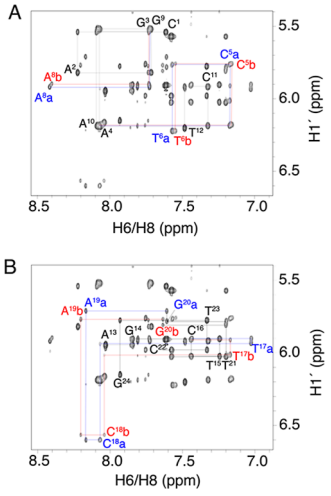

Figure 2. ^{1}H NOESY spectrum of 5′-d-($C^1A^2G^3A^4C^5T^6\underline{X}^7A^8G^9A^{10}C^{11}T^{12}$)-3′:5′-d-($A^{13}G^{14}T^{15}C^{16}T^{17}C^{18}A^{19}G^{20}T^{21}C^{22}T^{23}G^{24}$)-3′ (X = reduced PIX-AP site conjugate) showing sequential NOEs between aromatic pyrimidine H6 or purine H8 protons and deoxyribosyl H1′ protons. (A) The modified strand, showing nucleotides $C^1 \rightarrow T^{12}$. There is no aromatic proton on PIX showing an NOE with a deoxyribosyl proton in this region of the ^{1}H spectrum. (B) The complementary strand, showing nucleotides $A^{13} \rightarrow G^{24}$. The spectrum was acquired at 900 MHz, at 250 ms mixing time. The temperature was 288 K.

($C^1A^2G^3A^4C^5T^6\underline{X}^7A^8G^9A^{10}C^{11}T^{12}$) (X = reduced PIX-AP site conjugate) containing the reduced PIX-AP site conjugate, a continuous set of sequential NOEs of normal intensities was observed from C^1 to T^6. There was an interruption in the sequential NOEs between the T^6 H6 and T^6 H1′ protons. Two sets of sequential resonance signals were observed for nucleotides C^5, T^6 and A^8. ^{1}H COSY spectra afforded identification of ^3J COSY cross-peaks corresponding to vicinal couplings between the cytosine H5 and H6 protons in both the unmodified and modified duplexes. In agreement with the NOESY data, for the duplex containing the site-specific reduced pixantrone AP site conjugate, two COSY cross-peaks were observed for nucleotide C^{18} (Figure S1 in the Supporting Information). A continuous set of sequential NOEs of normal intensities was observed from and from A^8 to T^{12}. For the complementary strand 5′-d-($A^{13}G^{14}T^{15}C^{16}T^{17}C^{18}A^{19}G^{20}T^{21}C^{22}T^{23}G^{24}$)-3′, a continuous set of sequential NOEs was observed (Figure 2). Two sets of signals were resolved from T^{17} to G^{20}. The two NOEs between the T^{17} H1′ proton and the C^{18} H6 proton were of low intensity. The sequential NOEs from the C^{18} H1′ proton to the G^{24} H1′ proton were of normal intensities. The complete assignments of the deoxyribose H2′, H2″, and H3′ proton resonances were achieved. Most of the H4′ proton resonances were assigned. Partial assignments were made for the deoxyribose H5′ and H5″ proton resonances; these were in many instances overlapped precluding unequivocal assignments. The assignments of the DNA nonexchangeable protons are tabulated in Table S1 of the Supporting Information.

Exchangeable DNA Protons. Figure 3 shows ^{1}H spectra collected at 278 K in buffer containing 95:5 H_2O/D_2O, for the

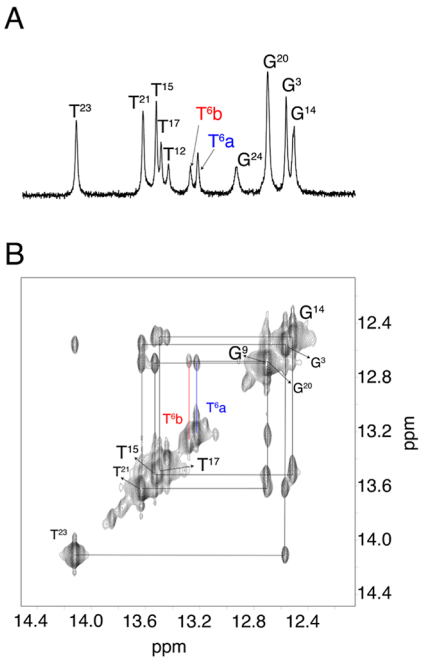

Figure 3. ^{1}H NMR of the modified duplex 5′-d-($C^1A^2G^3A^4C^5T^6\underline{X}^7A^8G^9A^{10}C^{11}T^{12}$)-3′:5′-d-($A^{13}G^{14}T^{15}C^{16}T^{17}C^{18}A^{19}G^{20}T^{21}C^{22}T^{23}G^{24}$)-3′ (X = reduced PIX-AP site conjugate). (A) The thymine N3H and guanine N1H imino protons. (B) NOESY spectrum showing sequential NOE connectivities for the imino protons. The imino proton signals from regioisomer R_a are in blue, while the imino proton signals from R_b are in red.

reduced PIX-AP site conjugate duplex 5′-d-($C^1A^2G^3A^4C^5T^6\underline{X}^7A^8G^9A^{10}C^{11}T^{12}$)-3′:5′-d-($A^{13}G^{14}T^{15}C^{16}T^{17}C^{18}A^{19}G^{20}T^{21}C^{22}T^{23}G^{24}$)-3′ (X = reduced PIX-AP site conjugate). The guanosine N1H and thymine N3H imino proton resonances were sharp in ^{1}H spectra collected at 278 K but broadened at higher temperatures. They were not observed at 298 K. The T^{12} N3H, T^{15} N3H, and T^{17} N3H imino resonances were partially resolved. The imino proton resonances were assigned using standard protocols;[68] a ^{1}H NOESY spectrum at 278 K is shown in Figure 3. The serial assignment T^{23} N3H → G^3 N1H → T^{21} N3H → G^{20} N1H → T^6 N3H, was obtained. The T^6 N3H imino proton appeared as two distinct signals. The serial T^6 N3H → C^{18} N3H → T^{17} N3H NOEs were not observed. The serial assignments T^{17} N3H → G^9 N1H → T^{15} N3H → G^{14} N1H were obtained. The terminal imino proton resonances C^1 N1H and T^{12} N3H were observed at δ 13.4 ppm and δ 12.9 ppm, respectively. They were broadened, presumably due to rapid exchange with water, in the NOESY spectrum. The T^{23} N3H resonance was assigned as the most downfield imino proton resonance (δ 14.1 ppm) because base pair A^2/T^{23} is flanked by two G/C pairs, which enhance its stacking interactions. The remaining

https://doi.org/10.1021/acs.biochem.6c00116
Biochemistry XXXX, XXX, XXX−XXX

Scheme 1. (A) Proposed Mechanism of Formation of R_a; (B) Proposed Mechanism of Formation of R_b

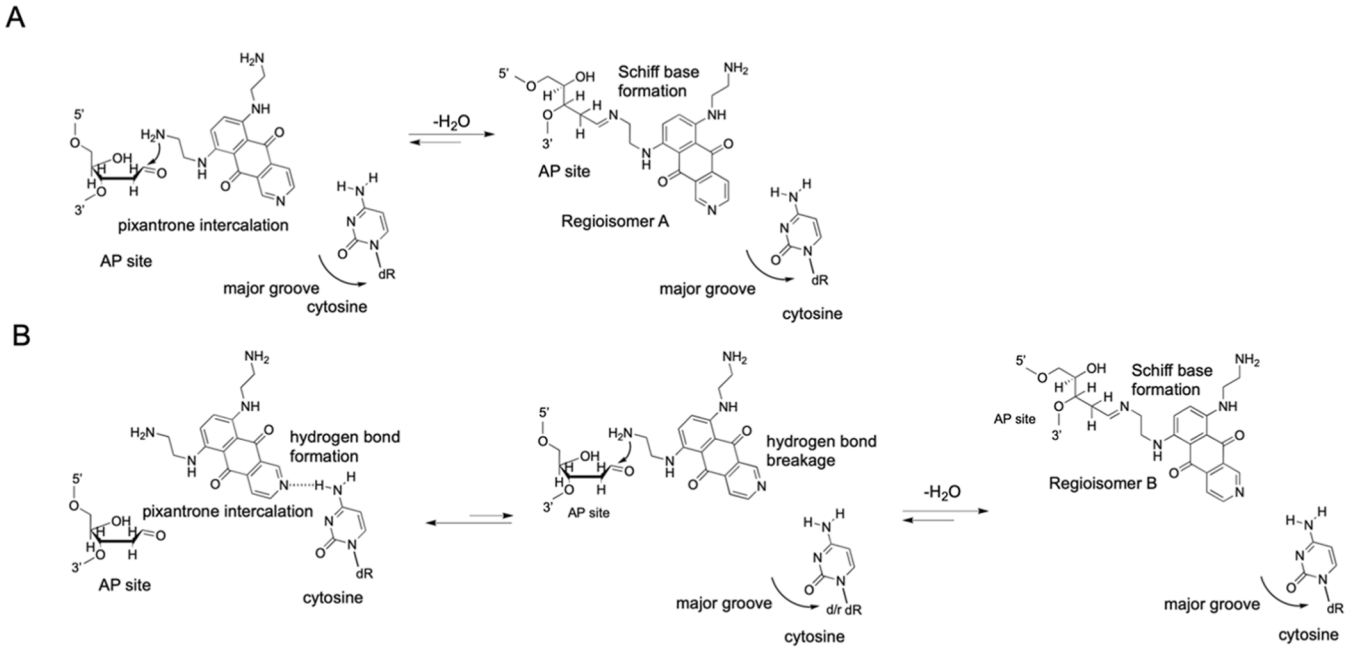

thymine imino protons, T^{12} N3H, T^{15} N3H, T^{17} N3H, and T^{21} N3H were within the anticipated δ 13.2−14.2 ppm range. The G^3 N1H, G^9 N1H, G^{14} N1H, G^{20} N1H, and G^{24} N1H imino proton resonances appeared in the anticipated δ 12.0−13.0 ppm range, characteristic of hydrogen-bonded G/C base pairs. G^{14} N1H (δ 12.4 ppm) was among the furthest upfield guanine resonances, indicating that the penultimate base pair C^{11}/G^{14} had weaker base stacking, probably due to its positioning between base pairs A^{10}/T^{15} and T^{12}/A^{13}, the latter being the terminal base pair. The chemical shift assignments for the exchangeable DNA protons are provided in Table S2 of the Supporting Information.

PIX Protons. These reduced PIX-AP site conjugates form by nucleophilic attack by the terminal amines of the 2-aminoethyl side chains of pixantrone on the transient C1′ aldehyde associated with epimerization of AP sites, followed by reduction of the resulting Schiff bases (Scheme 1). The aza-anthracenedione ring renders the two 2-aminoethyl side chains nonequivalent (Chart 1). The NMR data confirmed the presence of two regioisomers, labeled as R_a and R_b (Figure 4). For each, the H3 and H4 protons were defined as the aromatic protons on the nitrogen-containing portion of the aza-anthracenedione exhibiting ^3J coupling; the H1 protons were defined as the aromatic protons on the nitrogen-containing portion of the aza-anthracenedione not exhibiting ^3J coupling. The two regioisomeric H3 signals appeared at δ 8.67 and δ 8.77 ppm, while the two regioisomeric H1 signals appeared at δ 8.64 and δ 8.74 ppm, due to their proximity to the nitrogen atom. The two regioisomeric H4 signals were observed further upfield. The pixantrone H7 and H8 protons were located on the carbon-containing ring, exhibited chemical shifts of δ 7.68 and δ 7.79 ppm, respectively, and were nearly isochronous. The spectral assignments of R_a and R_b regioisomers were made from assessments of NOEs to DNA protons (Figure 5). The regioisomer R_a was assigned by two unique and strong NOEs. The first was between pixantrone H4 and the T^{17} methyl protons in the complementary strand, the 3′ neighboring base pair with respect to PIX. The second was between pixantrone

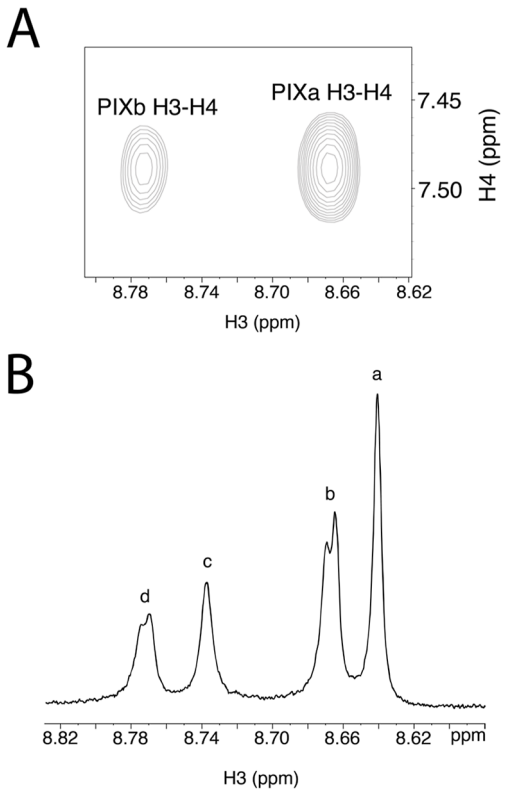

Figure 4. (A) ^{1}H COSY spectrum of the modified duplex 5′-d($C^1A^2G^3A^4C^5T^6\underline{X}^7A^8G^9A^{10}C^{11}T^{12}$)-3′:5′-d-($A^{13}G^{14}T^{15}C^{16}T^{17}C^{18}A^{19}G^{20}T^{21}C^{22}T^{23}G^{24}$)-3′ ($\underline{X}$ = reduced PIX-AP site conjugate) showing scalar couplings between PIX H3 and H4 protons arising from the two regioisomers R_a and R_b. The spectra were acquired at 900 MHz. The temperature was 288 K. (B) ^{1}H NMR spectrum showing the PIX H1, H3 protons arising from the regioisomeric reduced PIX-AP site conjugates R_a and R_b. The resonances are labeled a, R_a H1; b, R_a H3; c, R_b H1; d, R_b H3.

https://doi.org/10.1021/acs.biochem.6c00116
Biochemistry XXXX, XXX, XXX−XXX

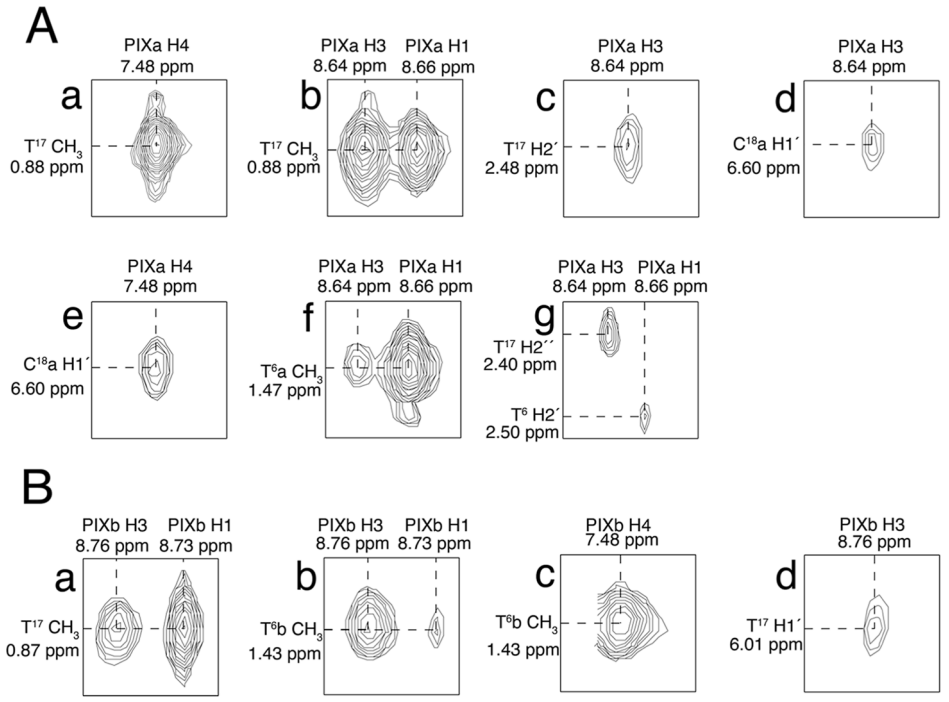

Figure 5. ^{1}H NOESY spectra of 5′-d(C^{1}A^{2}G^{3}A^{4}C^{5}T^{6}X^{7}A^{8}G^{9}A^{10}C^{11}T^{12})-3′:5′-d(A^{13}G^{14}T^{15}C^{16}T^{17}C^{18}A^{19}G^{20}T^{21}C^{22}T^{23}G^{24})-3′ (X = reduced PIX-AP site conjugate). (A) NOEs observed for regioisomer R_a with T^{6}, T^{17}, and C^{18} DNA protons. (B) NOEs observed for regioisomer R_b with T^{6}, and T^{17} protons. a, R_b T^{17} CH$_3$ → R_b X^{7} PIX H3; b, R_b T^{17} CH$_3$ → R_b X^{7} PIX H1; c, R_b T^{17} CH$_3$ → R_b PIX H6; d, R_b T^{6} CH$_3$ → R_b X^{7} PIX H3; e, R_b T^{6} CH$_3$ → R_b PIX H6; f, R_b T^{6} CH$_3$ → R_b X^{7} PIX H4; g, R_b T^{6} CH$_3$ → R_b C^{5} PIX H6; h, R_a T^{17} CH$_3$ → R_a X^{7} PIX H3; I, R_a T^{17} CH$_3$ → R_a X^{7} PIX H1; j, R_a T^{17} CH$_3$ → R_a X^{7} PIX H4; k, R_a T^{17} CH$_3$ → PIX H6; l, R_a T^{6} CH$_3$ → R_a X^{7} PIX H1; m, R_a T^{6} CH$_3$ → PIX H6; n, R_a T^{6} CH$_3$ → R_a C^{5} H6; o, T^{17} CH$_3$ → C^{16} H6.

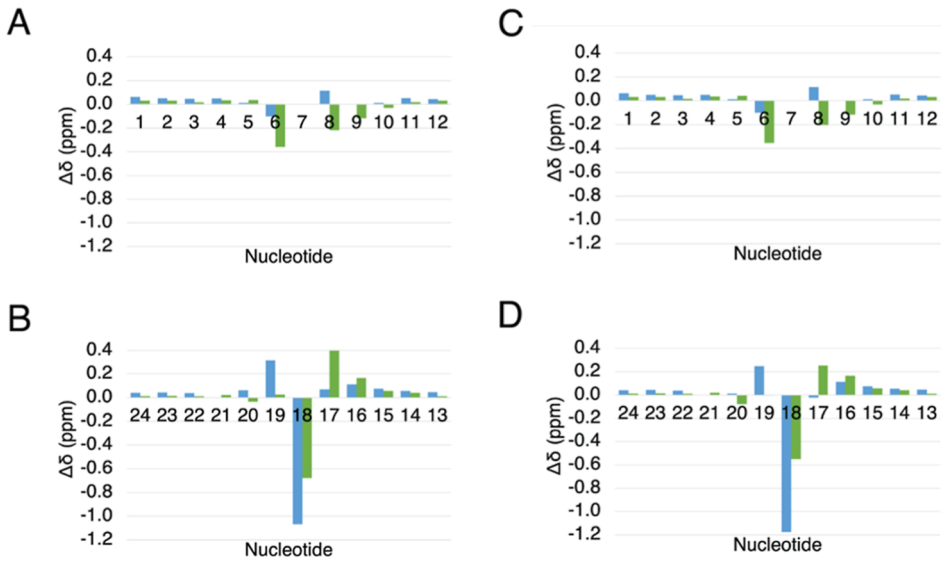

Figure 6. Chemical shift changes ($\Delta\delta$) of pyrimidine H6 or purine H8 base protons (green) and H1′ protons (blue) of 5′-d(C^{1}A^{2}G^{3}A^{4}C^{5}T^{6}X^{7}A^{8}G^{9}A^{10}C^{11}T^{12})-3′:5′-d(A^{13}G^{14}T^{15}C^{16}T^{17}C^{18}A^{19}G^{20}T^{21}C^{22}T^{23}G^{24})-3′ (X = reduced PIX-AP site conjugate) relative to the corresponding unmodified duplex. (A) Template strand of the modified duplex containing regioisomer R_a. (B) Complementary strands of the modified duplex containing regioisomer R_a. (C) Template strands of the modified duplex containing regioisomer R_b. (D) Complementary strand of the modified duplex containing regioisomer R_b.

H1 and the T^{6} methyl protons, the 5′ neighboring nucleotide of PIX. These implied R_a was intercalated, bringing the pixantrone H1 proton proximate to the T^{6} methyl protons, and bringing pixantrone H4 proximate to the T^{17} methyl protons. For R_b, a unique and strong NOE was observed between pixantrone H4 and the T^{6} methyl protons. This implied pixantrone H4 intercalated and was proximate to the T^{6} methyl protons. Both regioisomers displayed NOEs between the pixantrone H3 proton and the T^{17} methyl protons, but the intensity of this NOE was stronger for R_a than that for R_b (Figure 5). This was consistent with the chemical shifts of the regioisomeric pixantrone H3−H4 signals. In each, the more upfield signal was assigned to R_a, as in this regioisomer, the H3 and H4 protons were positioned closer to the complementary

https://doi.org/10.1021/acs.biochem.6c00116
Biochemistry XXXX, XXX, XXX−XXX

cytosine, C^{18}. In contrast, for R_b, the H3 and H4 protons were oriented toward the major groove, resulting in a greater chemical shift compared to R_a. The relative populations of each regioisomer were determined from integration. The integration of the signals arising from R_a were greater than the integrations of the signals assigned to R_b. The ratio observed was 6:4 R_a/R_b.

Chemical Shift Perturbations

Figure 6 shows DNA chemical shift perturbations induced in the 5′-d($C^1A^2G^3A^4C^5T^6\underline{X}^7A^8G^9A^{10}C^{11}T^{12}$)-3′:5′ d-($A^{13}G^{14}T^{15}C^{16}T^{17}C^{18}A^{19}G^{20}T^{21}C^{22}T^{23}G^{24}$)-3′ duplex, relative to the corresponding unmodified duplex. For both regioisomers R_a and R_b, substantial changes occurred at the modified base pair X^7/C^{18} and its immediate flanking 5′ and 3′neighbor base pairs. The greatest perturbations for both R_a and R_b were observed for the C^{18} nucleobase, which was complementary to the modified X^7 nucleotide. In the unmodified duplex, the regioisomeric C^{18} H5−H6 COSY crosspeaks were observed at δ 5.68 and δ 7.40 ppm, respectively. For the reduced PIX-AP site conjugate duplex, the regioisomeric C^{18} H5 signals were observed at δ 6.17 and δ 6.21 ppm, and the two H6 signals were observed at δ 8.05 and δ 8.08 ppm. For the R_a regioisomer, C^{18} H6 shifted downfield by δ 0.68 ppm; for R_b, C^{18} H6 shifted downfield by δ 0.55 ppm. The R_a C^{18} H5 proton also shifted downfield by δ 0.50 ppm and the R_b C^{18} H5 proton shifted downfield by δ 0.45 ppm. These chemical shifts are visible in Figure 5. There were also large downfield shifts observed for the anomeric protons of each regioisomer. For R_a, C^{18} H1′ shifted downfield by δ 1.07 ppm; for R_b, C^{18} H1′ shifted downfield by δ 1.18 ppm. Among the neighboring nucleotides displaying two subspectra due to the presence of the regioisomeric R_a and R_b conjugates, the 5′-neighboring nucleotide T^{17} H6 proton showed the greatest difference in chemical shift. The $\Delta\delta$ shift for T^{17} H6 was δ 0.40 ppm in the R_a-modified duplex and δ 0.25 ppm in the R_b-modified duplex. Chemical shift perturbations were also observed for the PIX protons. The PIX H3 and H4 protons were defined as the aromatic protons on the nitrogen-containing portion of the aza-anthracenedione exhibiting ^3J coupling; the H1 protons were defined as the aromatic protons on the nitrogen-containing portion of the aza-anthracenedione not exhibiting ^3J coupling.

Regioisomeric Reduced PIX-AP Site Conjugates

A series of reactions was conducted in 5′-d(CAGACT$\underline{X}$AGACT)-3′:5′-d(AGTCTCAGTCTG)-3′ ($\underline{X}$ = reduced PIX-AP site conjugate) as a function of temperature (Figure 7). At 0 °C, the ratio of regioisomers as determined by NMR was R_a/R_b = 1.8:1 after 30 min of incubation. No further changes were noted at longer incubation times. At 30 min of incubation at 35 °C, the ratio decreased to 1.5:1. At 35 °C, the ratio remained 1.5:1. At 60 °C, above the T_m for this duplex, the ratio decreased to 1.1:1. MALDI-TOF mass spectrometry confirmed the disappearance of residual AP site-containing duplex upon MX treatment (Figure S2 in the Supporting Information). Pixantrone was then reacted with the single strand 5′-d(CAGACT$\underline{X}$AGACT)-3′3′ containing an AP site. In these reactions, the R_a/R_b ratio remained at 1:1, irrespective of incubation temperature (Figure 7). These data suggested that in dsDNA formation of regioisomer R_a was favored. A series of reactions were incubated at 0.5, 1, and 3 h, both at 0 and 35 °C. At 60 °C, complete reaction within 1 h was observed (Figure S3 in the Supporting Information). At both 0 and 35 °C, the ratio R_a/R_b remained constant when the reactions were quenched at each time point (Figure S4 in the Supporting Information).

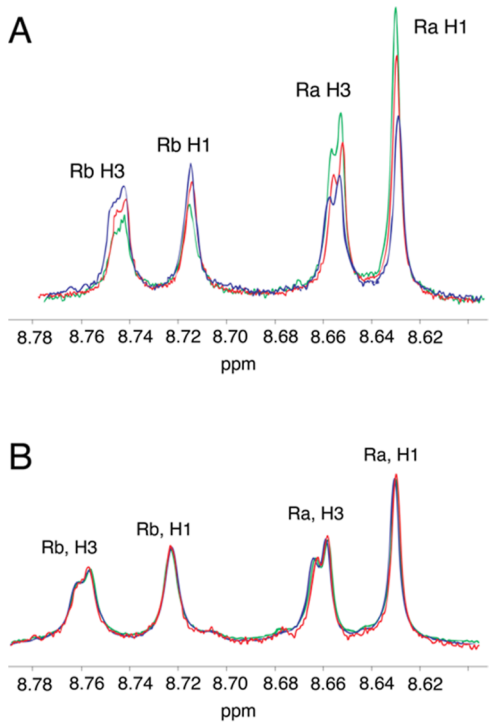

Figure 7. Overlay of ^{1}H NMR spectra of the PIX H1 and H3 protons in 5′-d($C^1A^2G^3A^4C^5T^6\underline{X}^7A^8G^9A^{10}C^{11}T^{12}$)-3′:5′-d-($A^{13}G^{14}T^{15}C^{16}T^{17}C^{18}A^{19}G^{20}T^{21}C^{22}T^{23}G^{24}$)-3′ ($\underline{X}$ = reduced PIX-AP site conjugate) prepared either in dsDNA or ssDNA. (A) Synthesized in AP-containing dsDNA, incubated at 0 °C (green), 35 °C (red), and 60 °C (blue). (B) Synthesized in ssDNA, incubated at 0 °C (green), 35 °C (red), and 60 °C (blue). The reaction time was for 30 min.

Unbiased MD Simulations of the Reduced PIX-AP Site Conjugates

To elucidate whether the position of the asymmetric isoquinoline N2 nitrogen of PIX would influence formation of the intercalated PIX-DNA system, we conducted simulations where PIX was covalently conjugated with the AP site. Two regioisomeric models were constructed of R_b or R_a (Figure 8). The intercalation process followed a similar mechanism for both regioisomers where PIX must reorient the

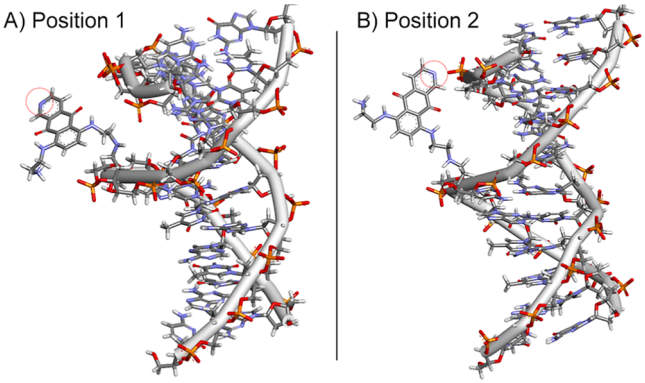

Figure 8. Starting positions of the reduced PIX-AP site conjugate with DNA for unbiased MD calculations. The regioisomeric difference is observed in the red circles showing the positions of the asymmetric N2 atoms .

https://doi.org/10.1021/acs.biochem.6c00116
Biochemistry XXXX, XXX, XXX−XXX

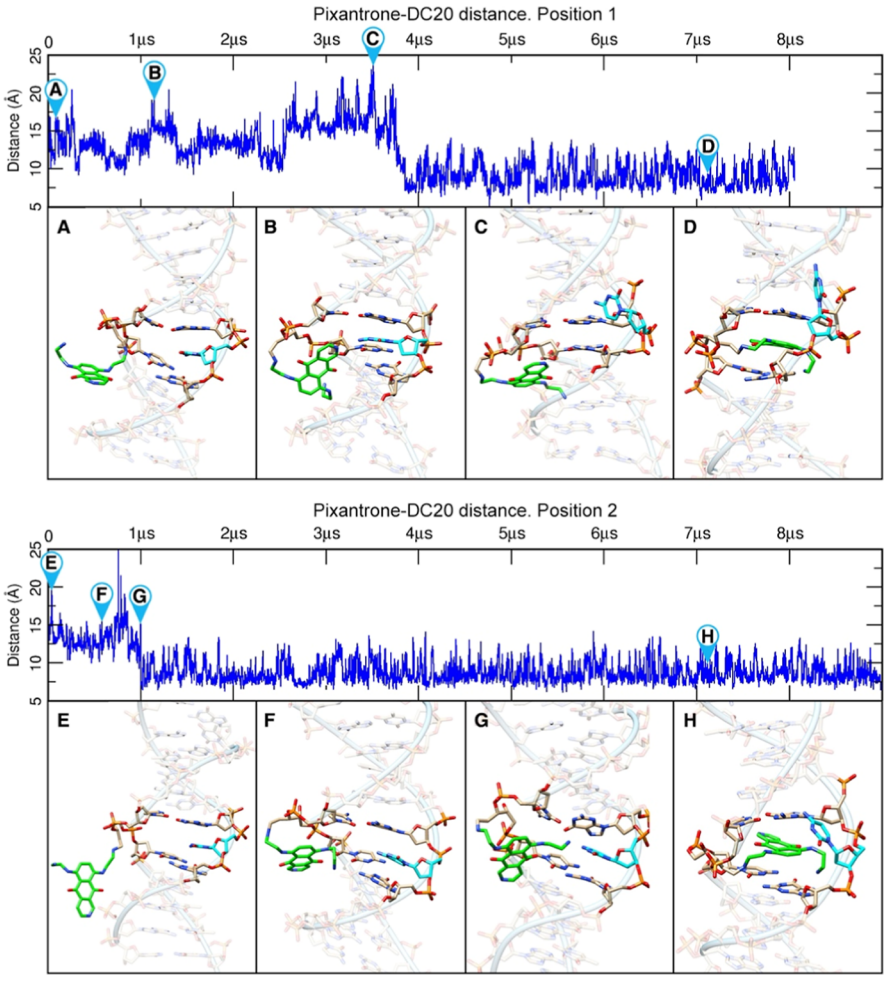

Figure 9. Unbiased MD calculation of the reduced PIX-AP site conjugate with DNA. Distance between the center of mass of PIX and cytosine 20. Panels A through H—selected frames from the trajectory to visualize the progress of the simulation. PIX is in green, unmatched cytosine 5 is in cyan.

aromatic component within the minor groove (Figure 9, panels B and F). As the simulations progressed, the bulge caused by the AP site allowed the unmatched cytosine base to freely rotate toward the solvent, exposing the gap between base-pairs C^8/G^{19} and C^5/G^{21} (Figure 9). Visual inspection of the MD trajectories suggested this step as the principal reorientation required to produce the final intercalated adduct. Exposing the gap caused by the flipping of C^{20} allowed PIX to insert in the resulting cavity, forming stacking interactions within the gap (Figure 9, panels D and H) and stabilizing with hydrogen bonds of the backbone at C^8, G^{19} and G^{21} (Figure 10). All five independent simulations produced a similar PIX-DNA intercalated structure that included the unmatched cytosine flipped toward the major groove. No discernible difference was detected if the PIX asymmetric N2 atom started in either position 1 (R_b) or position 2 (R_a). Binding energy analysis showed energies for position 1 (R_b) and position 2 (R_a) of the intercalated structures of −102.2 (±8.3) and −108.1 (±9.7) kcal/mol, respectively. The event that was required to form the final intercalated structure was the flipping of the cytosine residue. Once it shifted conformation toward the major groove, the PIX readily inserted the isoquinoline ring within the cavity.

Melting Temperature Analyses

Monophasic melting transitions were observed for both the 5′-d(CAGACTXAGACT)-3′:5′-d(AGTCTCAGTCTG)-3′ (X = reduced PIX-AP site conjugate, or THF) and as well, for the unmodified duplex (Figure 11). The T_m of the unmodified duplex 5′-d(CAGACTGAGACT)-3′:5′-d-(AGTCTCAGTCTG)-3′was 58.8 °C. The THF containing duplex 5′-d(CAGACTXAGACT)-3′:5′-d-(AGTCTCAGTCTG)-3′ (X = THF), which mimics an AP site, had a T_m of 37.2 °C. All the samples for melting temperature analyses were at 5 μM. Incorporation of the reduced PIX-AP site conjugate 5′-d(CAGACTXAGACT)-3′:5′-d(AGTCTCAGTCTG)-3′ (X = reduced PIX-AP site conjugate), stabilized the AP site relative to the THF-containing duplex; the T_m of the reduced PIX-AP site conjugate conjugate was 47.6 °C. This resulted in a 10.4 °C increase in the T_m, but destabilized DNA compared to the unmodified form and resulted in a 11.2 °C reduction in the T_m.

Structural Refinement

NOEs Between Regioisomeric Pixantrone AP site Conjugates and DNA. For both regioisomers, nucleotides C^5, T^6, A^8, and T^{17}, C^{18}, A^{19}, G^{20} in the complementary strand close to the PIX-AP site conjugate showed subspectra arising from the two regioisomers (Figure 5). NOEs from those nucleotides were critical for differentiating the two subspectra defining the regioisomeric PIX-AP site conjugates. Strong intranucleotide NOE cross-peaks between H3 and H4 were observed for both regioisomers (Figure 4). For internucleotide

https://doi.org/10.1021/acs.biochem.6c00116
Biochemistry XXXX, XXX, XXX−XXX

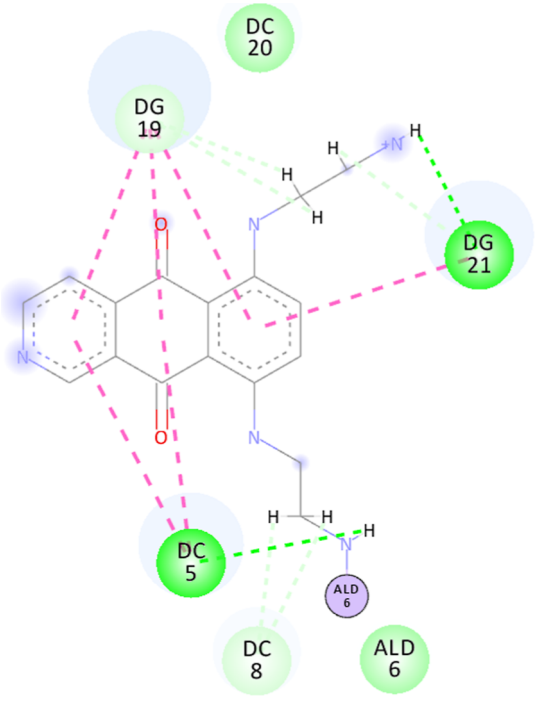

Figure 10. Specific interactions of the reduced PIX-AP site conjugate regioisomer R_a in the intercalated structure.

NOEs, R_a exhibited interactions between PIX protons H1, H3, and H4 with protons on T^6, T^{17}, and C^{18} (Figure 5). In contrast, R_b showed NOEs between PIX protons H1, H3, and H4 with T^6 and T^{17} but not with C^{18} (Figure 5).

Distance Restraints. The reduced PIX-AP site conjugates exist as a mixture of R_a and R_b regioisomers. To correct for this, intensities of NOEs observed for the R_a and R_b regioisomers were corrected by the ratio of regioisomers. The number of NOE-derived distance restraints from nonexchangeable protons calculated using MARDIGRAS[47] was 189 for R_a and 185 for R_b. These restraints were critical for defining structural differences between the two regioisomeric duplexes. For R_a, 85 intranucleotide distance restraints, 91 internucleotide distance restraints, and 13 reduced PIX-AP-site conjugate specific restraints were identified. For R_b, 85 intranucleotide, 89 internucleotide, and 11 reduced PIX-AP-site conjugate specific distance restraints were obtained. For both R_a and R_b, 30 empirical Watson−Crick H-bonding restraints, 100 backbone torsion angle restraints, and 70 deoxyribose pseudorotation restraints were employed, based on the canonical B-DNA structure.[48] Structural perturbations introduced by the reduced PIX-AP site conjugates affected base pairs T^6/A^{19}, X^7/C^{18}, and A^8/T^{17}. For both R_a and R_b canonical B-DNA restraints were not employed for nucleotides T^6, X^7, A^8, T^{17}, C^{18}, and A^{19}, or for the terminal nucleotides C^1, T^{12}, A^{13}, and G^{24}. In total, for R_a and R_b, 394 and 390 experimental and canonical restraints were applied, respectively. The independent application of distance restraints for R_a and R_b ensured accurate structural determination of both conjugate duplexes. The complete list of restraints is provided in Tables S3 and S4 of the Supporting Information.

Restrained Molecular Dynamics (rMD) Calculations

For structural refinement, initial models were constructed using MOE,[49] followed by unrestrained potential energy minimization to relieve steric strain, particularly around the

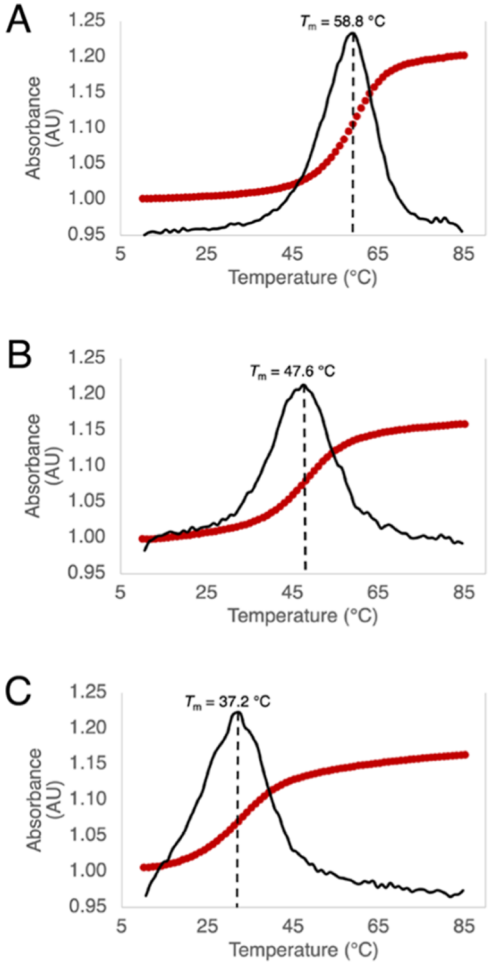

Figure 11. Thermal melting curves as recorded by absorbance at 260 nm. (A) The unmodified 5′-d(CAGACTXAGACT)-3′:5′-d-(AGTCTCAGTCTG)-3′duplex. (B) The modified 5′-d-(CAGACTXAGACT)-3′:5′-d(AGTCTCAGTCTG)-3′ (X = reduced PIX-AP site conjugate) duplex. (C) The modified 5′-d-(CAGACTXAGACT)-3′:5′-d(AGTCTCAGTCTG)-3′ (X = THF) duplex. Melting curves are dotted-lines in red, first derivatives of melting curves are continuous-lines in black.

bulky PIX moieties. These were further processed in xLEAP,[50] with partial charges calculated using the B3LYP/6-31G* basis set in GAUSSIAN.[28] A series of 100 ps rMD calculations were performed independently for each regioisomer using a simulated annealing protocol.[51,53] For both R_a and R_b, experimental and canonical restraints were applied with a force constant of 30 kcal mol^{-1} $Å^{-2}$ (Tables 1 and 2). Potential energy minimizations were performed using both steepest descent and conjugate gradient algorithms. The potential energy minimized structures were then used as the new starting structures, as pocket formation and unwinding were observed in the modification region. The coordinate and topology files were regenerated in xLEAP following the same protocol.[50] Each of the 20 emergent structures for R_a and R_b underwent further potential energy minimization using the steepest descent algorithm followed by conjugate gradients. The rMD calculations for each regioisomer converged, producing 20 energy minimized structures that were used to generate an average structure via the program SUPPOSE.[51]

For R_a, the average structure had a rms pairwise difference (rmsd) of 1.25 Å compared to the 20 individual structures. An

https://doi.org/10.1021/acs.biochem.6c00116
Biochemistry XXXX, XXX, XXX−XXX

Table 1. NMR Restraints Used for the R_a/R_b-Modified Duplex Structural Refinement

	R_a	R_b
internucleotide restraints	122	117
intranucleotide restraints	109	99
PIX-AP restraints	11	9
total NOE restraints	231	216
backbone torsion angle restraints	85	85
hydrogen bonding restraints	35	35
deoxyribose pseudorotation restraints	80	80
total number of restraints	431	416
number of distance restraints violations	17	15
number of distance restraints violations	6	6
total distance penalty/maximum penalty (kcal/mol)	128.768/10.315	117.110/8.267
total torsion angle penalty/maximum penalty (kcal/mol)	2.0345/0.087	2.167/0.071
rms distances (Å)	0.0213	0.0189
rms angles (deg)	2.760	2.560
distance restraint force field (kcal/mol/Å^2)	30	30
torsion angle restraint force field (kcal/mol/deg^4)	30	30

Table 2. RMS Differences and Sixth Root Residual (R^X_1) Values for the Average Structures of the R_a/R_b-Modified Duplex Emergent from rMD Calculations

	R_a	R_b
greatest RMS pairwise difference between 20 structures (Å)	1.25	1.02
greatest RMS difference from the average structures (Å)	1.06	0.097
sixth root residual R^X_1[a] calculated for the intranucleotide distances in the average structure, using CORMA[b]	0.0663	0.0703
sixth root residual R^X_1[a] calculated for the internucleotide distances in the average structure, using CORMA[b]	0.0675	0.0687
sixth root residual R^X_1[a] calculated for all distances in the average structure, using CORMA[b]	0.071	0.069
average error[c]	0.00089	0.00081

[a] R^X_1 is the sixth root R factor $\Sigma[((I_o)_i^{1/6}) - ((I_c)_i^{1/6}\Sigma((I_o)_i^{1/6}]$. [b] Mixing time was 250 ms. [c] Average error: $\Sigma(I_c - I_n)/n$, where I_c is NOE intensities calculated from the refined structure, and I_n is experimental NOE intensities.

overlay of these energy-minimized structures with the average minimized structure is shown in Figure 12. The structural analysis revealed that R_a intercalated into the duplex, with the complementary C[18] nucleotide extruded into the major groove. For R_b, the average structure had a pairwise rmsd of 1.02 Å, with its overlay also shown in Figure 12. For both regioisomers, base pair fraying was observed at the terminal regions at 288 K, leading to reduced convergence at the duplex ends.

Complete Relaxation Matrix Analysis

The accuracy of the average energy-minimized structures for R_a and R_b was evaluated using complete relaxation matrix analysis in CORMA.[47] For R_a, all intra- and internucleotide sixth root residuals R^X_1 were equal to or less than 0.1, confirming an excellent agreement between the calculated and experimental NOE distances (Figure 13). The average R^X_1 values for intranucleotide and internucleotide interactions were 0.0663 and 0.0675, respectively, indicating that the structures were in reasonable accordance with NOE data. For R_b, a similar evaluation was performed. The individual intra- and internucleotide R^X_1 values were also ≤0.1, suggesting excellent agreement with the experimental data (Figure 13). The average R^X_1 values for intranucleotide and internucleotide interactions were 0.0703 and 0.0687, respectively. The overall R^X_1 value for R_b was 0.0690. The complete relaxation matrix analysis confirmed that both regioisomeric structures were in reasonable agreement with the NOE-derived distance restraints. To assess consistency between model and experiment, CORMA analysis was performed. R^X_1 values of all nucleotides were less than 0.1, indicating excellent agreement between calculated and experimental NOEs. To ensure that the observed difference was not an artifact of starting structure bias, simulated annealing calculations were repeated using cross-swapped minimized inputs (R_a's energy-minimized structure was used for R_b's protocol and vice versa). In both cases, the systems converged to similar final structures, with R_b consistently intercalated more deeply into DNA duplex than R_a.

Figure 12. Overview of the 20 lowest energy violation structures generated from rMD calculations of (A) R_a-modified duplex, and (B) R_b-modified duplex, 5′- d(CAGACTXAGACT)-3′:5′-d-(AGTCTCAGTCTG)-3′ (X = PIX-AP), carried out using a simulated annealing protocol and experimental NOEs generated distance restraints.

https://doi.org/10.1021/acs.biochem.6c00116
Biochemistry XXXX, XXX, XXX−XXX

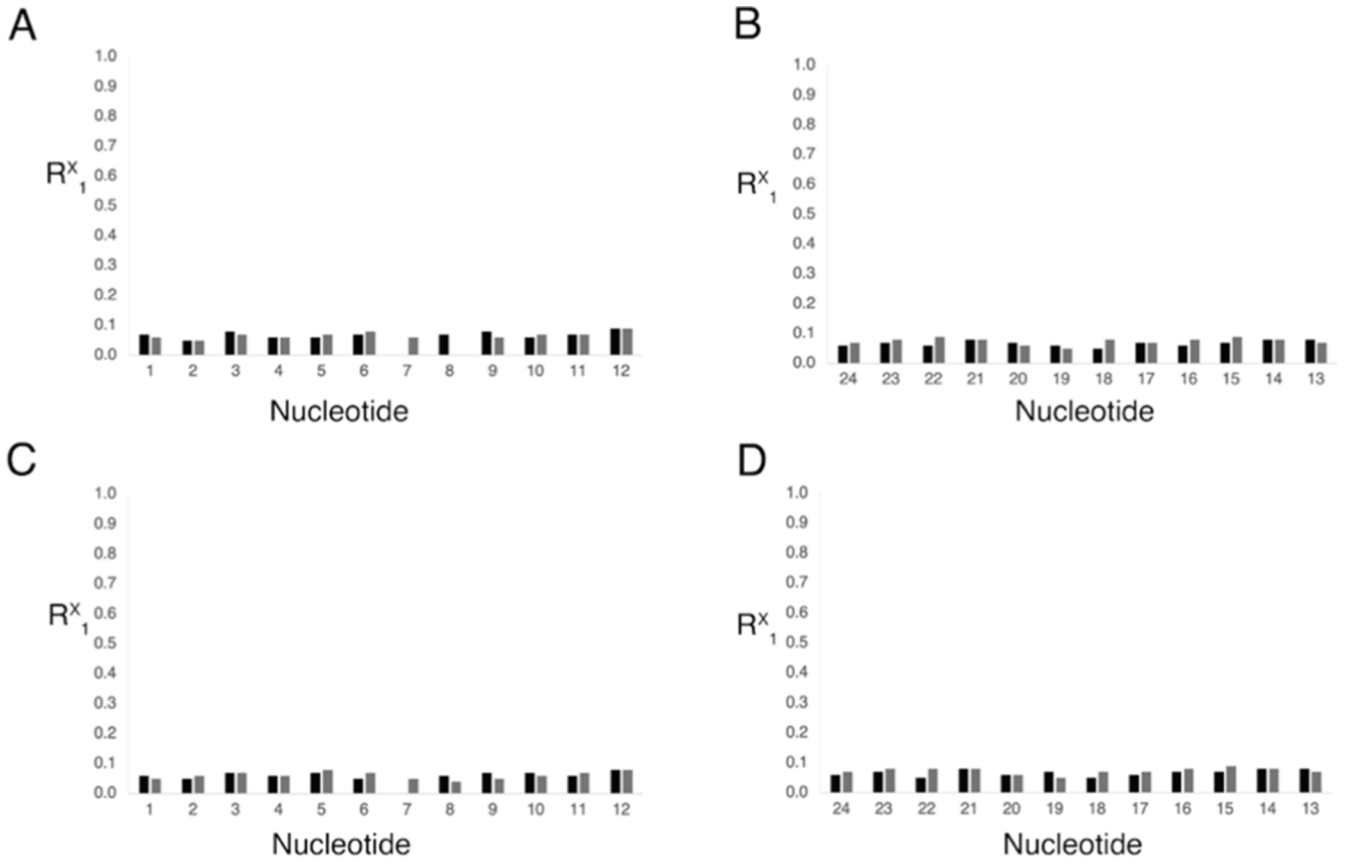

Figure 13. Calculation of sixth root residual values (R^X_1) between theoretical NOEs predicted by complete relaxation matrix calculations and experimental NOEs for the averaged refined structure of 5′-d(CAGACTXAGACT)-3′:5′-d(AGTCTCAGTCTG)-3′ (X = PIX-AP) emergent from the rMD calculations, using CORMA. (A) The R^X_1 values of intranucleotide and internucleotide NOEs in the R_a-modified strand. (B) The R^X_1 values of intranucleotide and internucleotide NOEs in the R_a-modified complementary strand. (C) The R^X_1 values of intranucleotide and internulceotide NOEs in the R_b-modified strand. (D) The R^X_1 values of internucleotide and intranulceotide NOEs in the R_b-modified complementary strand. The intranucleotide NOE residuals are colored in black. The internucleotide NOE residuals are colored in gray.

Structures of Regioisomeric Reduced PIX-AP Site Conjugate Duplexes

Figure 14 presents views of R_a and R_b. Both intercalated into the DNA. For R_a, the reduced PIX-AP site conjugate intercalated with the pixantrone N2 and H3 atoms facing into the major groove. The complementary C^{18} was extruded into the major groove, making space for the PIX-AP site conjugate. Structural perturbations were localized at base pair X^7/C^{18} and its 5′- and 3′-flanking base pairs, T^6/A^{19} and A^8/T^{17}. The flanking base pairs maintained Watson−Crick H-bonding. For R_b, the PIX-AP conjugate also intercalated into the DNA, but with a key difference. The asymmetric PIX N2 atom was positioned toward the displaced C^{18} and was intercalated more deeply. Like in R_a, C^{18} was also extruded from the duplex into the major groove, making space for the reduced PIX-AP site conjugate. The PIX N2 and H3 protons still faced toward the major groove, but the overall intercalation depth was deeper compared to R_a (Figure 14). Overall structural perturbations were similar, primarily affecting X^7/C^{18}, T^6/A^{19}, and A^8/T^{17}, while the flanking base pairs retained Watson−Crick H-bonding.

Crystal Structure of a PIX-Modified DNA Dodecamer

The crystal structure of the modified DDD 5′-d-$(C^1G^2C^3X^4A^5A^6T^7T^8C^9G^{10}C^{11}G^{12})$-3′ with a PIX-AP conjugate (X^4) in place of G was determined by Br-SAD and refined to a resolution of 2.5 Å. X-ray crystallography revealed that

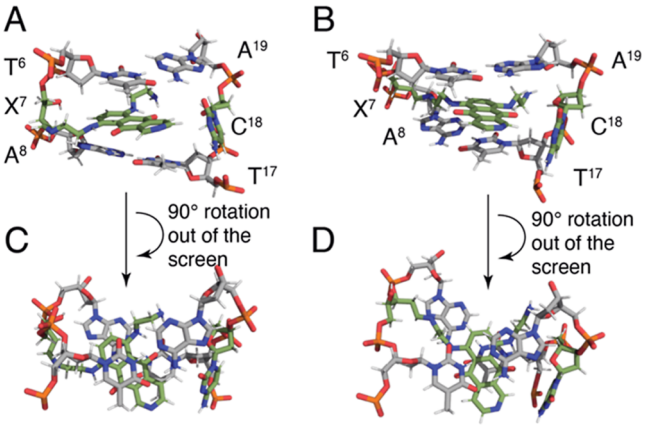

Figure 14. Base stacking of 5′-d(CAGACTXAGACT)-3′:5′-d-(AGTCTCAGTCTG)-3′ (X = reduced PIX-AP site conjugate), showing base pairs T^6/A^{19}, X^7/C^{18}, and A^8/T^{17}, derived from the 20 lowest-energy structures from restrained MD calculations. The reduced PIX-AP site conjugates are green; other DNA bases are gray. (A) View from the major groove of the duplex containing regioisomer R_a. (B) View from the major groove of the duplex containing regioisomer R_b. (C) Top-down view of panel A rotated 90° outward from the screen. (D) Top-down view of panel B rotated 90° outward from the screen.

https://doi.org/10.1021/acs.biochem.6c00116
Biochemistry XXXX, XXX, XXX−XXX

replacing a guanine with the PIX-AP conjugate induces an abrupt structural kink, causing the DNA strands to form independent infinite duplexes connected by a perpendicular crossover duplex. Within these connector duplexes, the pixantrone (PIX) moieties do not intercalate into the DNA as traditionally expected; instead, they are flipped relative to one another in an extrahelical orientation and sandwiched between alternating C/G dimers to maximize stacking interactions. Selected crystal data, data collection parameters and final refinement parameters and deviations from ideal geometries are listed in Table S5 of the Supporting Information and the quality of the final electron density is depicted in Figure S5 of the Supporting Information. For a detailed description of the crystal structure see the Results and Discussion in the Supporting Information, and Figures S5−S8 in the Supporting Information.

DISCUSSION

Pixantrone,[69−71] approved in the European Union for the treatment of relapsed or refractory aggressive B-cell non-Hodgkin lympohoma,[72,73] was designed to reduce redox cycling associated with mitoxantrone, by eliminating the hydroquinone moiety.[74,75] While PIX exhibits reduced cellular uptake as compared to MTX, it does not form stable Fe^{3+} complexes and shows minimal redox activity in cardiac tissue.[76] The observation that PIX does not inhibit the topoisomerase IIb isoform found in cardiac tissues may also be a factor in its reduced cardiotoxicity as compared to MTX.[25] More recently, Bellamri et al.[21] demonstrated that amino groups of doxorubicin (DOX), MTX, and PIX may react with AP sites to form Schiff base conjugates. PIX differs from DOX or MTX since the presence of the asymmetric N2 nitrogen in PIX renders the (2-aminoethyl)amino side chains nonequivalent. Consequently, unlike DOX or MTX, PIX has the potential to form regioisomeric PIX-AP site Schiff base conjugates.

Regioisomeric PIX-AP Site Schiff Base Conjugates

Our results confirm that PIX forms regioisomeric Schiff base conjugates with AP sites in DNA, designated as regioisomers R_a and R_b (Figure 2). The reduced forms of these regioisomeric Schiff base conjugates are differentiated by their distinct patterns of ^{1}H NOEs in NMR spectroscopy (Figure 5). Regioisomer R_a exhibits a unique strong NOE between PIX H4 and the T^{17} methyl protons in the complementary strand, the 3′ neighboring base pair with respect to PIX, as well as an NOE between PIX H1 and the T^6 methyl protons, the 5′ neighboring nucleotide of PIX. The presence of these NOEs implies that for regioisomer R_a PIX is intercalated, bringing the PIX H1 proton proximate to the T^6 methyl protons, and bringing PIX H4 proximate to the T^{17} methyl protons. In contrast, regioisomer R_b may be identified by a unique strong NOE between PIX H4 and the T^6 methyl protons (Figure 5B). This implies that for regioisomer R_b, PIX also intercalates, with PIX H4 proximate to the T^6 methyl protons. Both regioisomers display NOEs between the PIX H3 proton and the T^{17} methyl protons, but with different intensities, that for R_a being stronger (Figure 5). This is consistent with chemical shifts of the regioisomeric PIX H3−H4 signals (Figure 4). For R_a PIX H3−H4 is the more upfield signal as in this regioisomer, the H3 and H4 protons are closer to the complementary cytosine, C^{18}. In contrast, for R_b, the PIX H3 and H4 protons orient toward the major groove, resulting in a greater chemical shift compared to R_a.

Regioisomeric Selectivity of PIX Intercalation into dsDNA

The 6:4 R_a/R_b ratio of regioisomeric Schiff base conjugates in dsDNA observed by integration of NMR signals was unexpected. The PIX (2-aminoethyl)amino side chains are distal to the asymmetric isoquinoline N2 nitrogen and might be anticipated to exhibit similar reactivity regarding forming Schiff base conjugates at AP sites. The differential formation of regioisomeric products does not appear to result from a thermodynamic preference for the reduced R_a vs R_b regioisomers in dsDNA. The single-phase melting curves observed for the regioisomeric mixture of reduced PIX-AP site conjugates (Figure 11) indicates that in dsDNA neither regioisomeric product is favored thermodynamically. As well, unbiased MD simulations show that both regioisomeric conjugates have similar intercalation energetics.

Instead, the distribution of regioisomeric products R_a and R_b in dsDNA may be determined by the relative rates of reaction leading to formation of each regioisomer, modulated by differences in intercalative binding of PIX to DNA. The asymmetric structure of PIX allows two orientations for intercalation of the isoquinoline ring at an AP site in dsDNA. In forming the R_a regioisomer, upon intercalation into dsDNA, the PIX asymmetric nitrogen N2 faces outward from the DNA helix. Intercalation of PIX in this orientation positions its side chain amino group in alignment with the AP site (Scheme 1). Once intercalated, the PIX amino group may attack the transiently formed aldehyde at the AP site, forming a Schiff base conjugate. In contrast, in forming the R_b regioisomer, upon intercalation, the PIX asymmetric nitrogen N2 orients toward cytosine C^{18} opposite the AP site. It comes within H-bonding distance of C^{18}. When intercalated in this manner, an additional reorientation may be required before the PIX amino group can attack the AP site, forming the Schiff base conjugate. This may hinder formation of R_b in dsDNA. Significantly, in ssDNA containing an AP site, where the complementary cytosine C^{18} is absent, both regioisomers R_a and R_b form in equal proportions. Also, in dsDNA regioisomer R_a remains the predominant product if the reaction occurs below the T_m value of the dsDNA. Above the T_m value, regioisomer formation reverts to 1:1 R_a/R_b. Overall, regioisomer formation in dsDNA appears to be governed by the ability of the PIX asymmetric nitrogen atom N2 to interact with the complementary cytosine C^{18}. This represents one possible interpretation based on NMR-derived structural evidence and should be viewed as a plausible explanation rather than a definitive mechanistic conclusion.

Conformations of Reduced Regioisomeric Pixantrone-AP Site Conjugates

In both regioisomers the PIX isoquinoline ring stacks between neighboring base pairs, with the complementary C^{18} extruded into the major groove (Figure 14). The core dsDNA conformation is locally disrupted at the conjugated AP site and its flanking 5′ and 3′ neighboring base pairs, as evidenced by the observation that only C^5, T^6, A^8, T^{17}, C^{18}, A^{19}, and G^{20} exhibit two subspectra arising from the two regioisomers (Figures 2 and 3). Of the regioisomeric AP site conjugates R_b intercalates more deeply than R_a. Overall, both regioisomeric PIX-AP site conjugates thermally stabilize the AP-containing dsDNA duplex (Figure 11). While both regioisomeric conjugates display NOEs between PIX H3 and the T^{17} methyl protons (Figure 5), the PIX H3 proton is closer to the T^{17} methyl group in R_a vs R_b (Figure 14) and the corresponding

https://doi.org/10.1021/acs.biochem.6c00116
Biochemistry XXXX, XXX, XXX−XXX

magnitude of the NOE is greater (Figure 5). The positioning of the asymmetric isoquinoline ring nitrogen N2 governs intercalation depth of the R_a and R_b regioisomeric AP site conjugates. The deeper intercalation of R_b may result due to the propensity of the N2 nitrogen to transiently hydrogen bond with the exocyclic N^4-dC amino group, thus pulling the PIX ring deeper into the duplex DNA. Thus, the regioisomeric differences in PIX N2 positioning may govern formation of regioisomeric PIX-AP conjugates.

Anthracycline Antibiotics and Schiff Base Formation

AP sites in DNA are reactive electrophilic sites that may form covalent adducts with nucleophilic groups via a transiently formed aldehyde. The amino groups in anthracycline antibiotics are known to form covalent aminal linkages with DNA. In the presence of formaldehyde, the daunosamine N3′ amine of DOX conjugates via an aminal linkage with the exocyclic amino group of guanine in dsDNA; this chemistry facilitated crystallographic analyses of intercalated DNA-DOX adducts.[77−79] These conjugates interfered with transcription factors that recognize 5′-GpC-3′ sequences, ultimately triggering apoptosis.[80] PIX also forms aminal conjugates with the exocyclic amine of guanine in dsDNA in the presence of formaldehyde, in vitro.[81] This leads to the formation of interstrand cross-links (ICLs) (Scheme 1).[15,82−90] AP sites may generate stable interstrand cross-links (ICLs) with dA in dsDNA. Kellum et al.[16] characterized a β-*N*-glycosyl linkage between an N^6-dA amino group and an AP site.

Biological Implications

Anthracycline antibiotics are extensively used to treat various cancers due to their ability to disrupt cell division.[91,92] Their primary mechanism of action is believed to be mediated by topoisomerase II inhibition,[93,94] which leads to the induction of double-strand breaks, interference with DNA replication, and ultimately, cell death. Utilization of DOX and MTX in the clinic is limited by dose-dependent cardiotoxicity.[95,96] The source is not completely understood and possibly involves multiple factors. It has been linked to quinone−hydroquinone redox cycling,[97] and off-target collateral damage to the topoisomerase IIb isoform found in cardiac tissues.[25] Both DOX and MTX form Fe^{3+} complexes and generate hydroxyl radicals,[98−100] which promote iron-mediated oxidative stress.

The observation that PIX conjugates to AP sites in DNA as a mixture of regioisomeric products leads to the question as to whether R_a and R_b may be differentially recognized by DNA damage repair processes. Both regioisomeric reduced Schiff base conjugates are less thermodynamically stable compared to unmodified DNA, as shown by T_m studies (Figure 11), suggesting that PIX intercalation stabilizes the AP site but that the resulting Schiff base conjugate does not restore native dsDNA stability. This is consistent with reports that the Schiff base conjugates are reversible and have short lifetimes in dsDNA. Minko et al.[101] reported PIX exhibited weaker AP lyase activity and showed less inhibition of APE1 as compared to MTX, attributed to its lower binding affinity for AP site-containing DNA. The reduced Schiff base regioisomer R_b inserts more deeply into the dsDNA helix than does the regioisomer R_a. By comparison, the unique crystal structure observed for the DDD with PIX conjugated to AP sites at the G-tract/A-tract boundaries clearly supports the paramount role of stacking by the pixantrone anthracycline analog in organizing these conjugates.

Summary

PIX forms regioisomeric Schiff base conjugates with AP sites in dsDNA, differing in the position of the asymmetric isoquinoline nitrogen N2. R_a predominates in dsDNA due to a favorable intercalation alignment, while R_b forms more slowly, possibly due to the need to break a stabilizing hydrogen bond with the opposing cytosine. In ssDNA, both regioisomers form in equal amounts. Our results suggest that formation of PIX regioisomeric Schiff base conjugates is sensitive to DNA environment, such as the presence of unwound replication forks, or supercoiled regions, which may modulate formation of the two regioisomers.

■ ASSOCIATED CONTENT

Supporting Information

The Supporting Information is available free of charge at https://pubs.acs.org/doi/10.1021/acs.biochem.6c00116.

Supporting results and discussion for X-ray crystallographic studies, Tables S1, chemical shifts of non-exchangeable DNA protons; S2, chemical shifts (ppm) of exchangeable DNA protons; S3, NOE distance restraints of PIX-AP conjugate (R_a) DNA duplex used for rMD calculations in AMBER; S4, NOE distance restraints of PIX-AP conjugate (R_b) DNA duplex used for rMD calculations in AMBER; S5, selected crystal data, X-ray data collection and refinement parameters; and Figures S1, two-dimensional COSY spectra of PIX-AP conjugate duplex and unmodified duplex; S2, MALDI-TOF mass spectrum of the MX quenched reaction; S3, HPLC-UV chromatogram of the reaction of the AP-containing oligonucleotide with PIX reduced with $NaB(CN)H_3$ at 60 °C analyzed after 1 h; S4, HPLC-UV chromatogram of the reaction of the AP-containing oligonucleotide with PIX reduced with $NaB(CN)H_3$; S5, final Fourier $2F_o$-F_c sum electron density (green meshwork) around the C^3−PIX-A^5 base steps drawn at ∼1.1 σ threshold; S6, lattice interactions in the crystal structure of a modified DDD with a PIX-AP conjugate; S7, superimposition of yellow and green DDD strands with PIX-AP conjugates; S8, stacked PIX moieties alternating with CG dimers in the connector duplex (PDF)

■ AUTHOR INFORMATION

Corresponding Author

Michael P. Stone − *Department of Chemistry, Vanderbilt University, Nashville, Tennessee 37235, United States; Center for Structural Biology, Vanderbilt University, Nashville, Tennessee 37235, United States; Vanderbilt-Ingram Cancer Center, Vanderbilt University Medical Center, Nashville, Tennessee 37232, United States;* orcid.org/0000-0002-0922-0216; Phone: 615-322-2589; Email: michael.p.stone@vanderbilt.edu

Authors

Yizhi Fu − *Department of Chemistry, Vanderbilt University, Nashville, Tennessee 37235, United States*

John T. Terrell − *Department of Chemistry, Vanderbilt University, Nashville, Tennessee 37235, United States;* orcid.org/0000-0003-2947-1861

https://doi.org/10.1021/acs.biochem.6c00116
Biochemistry XXXX, XXX, XXX−XXX

Andrew Kellum − *Department of Chemistry, Vanderbilt University, Nashville, Tennessee 37235, United States*
Pradeep S. Pallan − *Department of Biochemistry, School of Medicine, Vanderbilt University, Nashville, Tennessee 37232, United States*
Rodrigo Galindo-Murillo − *Ionis Pharmaceuticals Inc., Carlsbad, California 92010, United States*
Carmelo J. Rizzo − *Department of Chemistry, Vanderbilt University, Nashville, Tennessee 37235, United States*
Martin Egli − *Department of Biochemistry, School of Medicine, Vanderbilt University, Nashville, Tennessee 37232, United States; Center for Structural Biology, Vanderbilt University, Nashville, Tennessee 37235, United States; Vanderbilt-Ingram Cancer Center, Vanderbilt University Medical Center, Nashville, Tennessee 37232, United States;* orcid.org/0000-0003-4145-356X

Complete contact information is available at: https://pubs.acs.org/10.1021/acs.biochem.6c00116

Funding

Funding provided by NIH grants R01 CA-55678, R01 ES-029357, and P01 CA-160032 (M.P.S., M.E., and C.J.R.) is gratefully acknowledged. The Vanderbilt-Ingram Cancer Center is funded by NIH grant P30 CA-068485. Funding for the NMR spectrometers was provided by in part by instrumentation grants S10 RR-05805, S10 RR-025677, and National Science Foundation Instrumentation Grant DBI 0922862, the latter funded by the American Recovery and Reinvestment Act of 2009 (Public Law 111−5). Vanderbilt University assisted with the purchase of NMR instrumentation. Funding for open access charge: National Institutes of Health. This research used resources of the Advanced Photon Source, a U.S. Department of Energy (DOE) Office of Science User Facility operated for the DOE Office of Science by Argonne National Laboratory under Contract No. DE-AC02-06CH11357. Use of the LS-CAT Sector 21 was supported by the Michigan Economic Development Corporation and the Michigan Technology Tri-Corridor (Grant 085P1000817).

Notes

The authors declare no competing financial interest.

REFERENCES

(1) Lindahl, T.; Nyberg, B. Rate of depurination of native deoxyribonucleic acid. *Biochemistry* **1972**, *11*, 3610−3618.
(2) Yudkina, A. V.; Zharkov, D. O. The hidden elephant: Modified abasic sites and their consequences. *DNA Repair (Amst)* **2025**, *148*, 103823.
(3) Taglialatela, A.; Ciccia, A. Endogenous Sources of Abasic Sites and Implications for DNA Replication: Mechanisms of Fork Stalling and Recovery. *Annu Rev Biochem* **2026**, *95*, 143−172.
(4) Nejad, M. I.; Johnson, K. M.; Price, N. E.; Gates, K. S. A new cross-link for an old cross-linking drug: The nitrogen mustard anticancer agent mechlorethamine generates cross-links derived from abasic sites in addition to the expected drug-bridged cross-links. *Biochemistry* **2016**, *55*, 7033−7041.
(5) Lindahl, T.; Ljungquist, S.; Siegert, W.; Nyberg, B.; Sperens, B. DNA N-glycosidases: properties of uracil-DNA glycosidase from Escherichia coli. *J. Biol. Chem.* **1977**, *252*, 3286−3294.
(6) Rahimoff, R.; Kosmatchev, O.; Kirchner, A.; Pfaffeneder, T.; Spada, F.; Brantl, V.; Müller, M.; Carell, T. 5-Formyl- and 5-carboxydeoxycytidines do not cause accumulation of harmful repair intermediates in stem cells. *J. Am. Chem. Soc.* **2017**, *139*, 10359−10364.
(7) Chen, H.; Yao, L.; Brown, C.; Rizzo, C. J.; Turesky, R. J. Quantitation of apurinic/apyrimidinic sites in isolated DNA and in mammalian tissue with a reduced level of artifacts. *Anal. Chem* **2019**, *91*, 7403−7410.
(8) Hoehn, S. T.; Turner, C. J.; Stubbe, J. Solution structure of an oligonucleotide containing an abasic site: evidence for an unusual deoxyribose conformation. *Nucleic Acids Res.* **2001**, *29*, 3413−3423.
(9) Chen, J.; Dupradeau, F. Y.; Case, D. A.; Turner, C. J.; Stubbe, J. DNA oligonucleotides with A, T, G or C opposite an abasic site: structure and dynamics. *Nucleic Acids Res.* **2008**, *36*, 253−262.
(10) Choi, J. Y.; Lim, S.; Kim, E. J.; Jo, A.; Guengerich, F. P. Translesion synthesis across abasic lesions by human B-family and Y-family DNA polymerases alpha, delta, eta, iota, kappa, and REV1. *J. Mol. Biol.* **2010**, *404*, 34−44.
(11) Patra, A.; Zhang, Q.; Lei, L.; Su, Y.; Egli, M.; Guengerich, F. P. Structural and kinetic analysis of nucleoside triphosphate incorporation opposite an abasic site by human translesion DNA polymerase eta. *J. Biol. Chem.* **2015**, *290*, 8028−8038.
(12) Manoharan, M.; Ransom, S. C.; Mazumder, A.; Gerlt, J. A.; Wilde, J. A.; Withka, J. A.; Bolton, P. H. The characterization of abasic sites in DNA heteroduplexes by site specific labeling with C-13. *J. Am. Chem. Soc.* **1988**, *110*, 1620−1622.
(13) Wilde, J. A.; Bolton, P. H.; Mazumder, A.; Manoharan, M.; Gerlt, J. A. Characterization of the equilibrating forms of the aldehydic abasic site in duplex DNA by O-17 NMR. *J. Am. Chem. Soc.* **1989**, *111*, 1894−1896.
(14) Gates, K. S. An Overview of Chemical Processes That Damage Cellular DNA: Spontaneous Hydrolysis, Alkylation, and Reactions with Radicals. *Chem. Res. Toxicol.* **2009**, *22*, 1747−1760.
(15) Dutta, S.; Chowdhury, G.; Gates, K. S. Interstrand cross-links generated by abasic sites in duplex DNA. *J. Am. Chem. Soc.* **2007**, *129*, 1852−1853.
(16) Kellum, A. H., Jr.; Qiu, D. Y.; Voehler, M. W.; Martin, W.; Gates, K. S.; Stone, M. P. Structure of a Stable Interstrand DNA Cross-Link Involving a *β*-N-Glycosyl Linkage Between an N6-dA Amino Group and an Abasic Site. *Biochemistry* **2021**, *60*, 41−52.
(17) Chan, W.; Jin, L. DNA-Protein Cross-Links Formed by Reacting Lysine with Apurinic/Apyrimidinic Sites in DNA and Human Cells: Quantitative Analysis by Liquid Chromatography-Tandem Mass Spectrometry Coupled with Stable Isotope Dilution. *Anal. Chem.* **2022**, *94*, 803−810.
(18) Bryan, C.; Yang, K. Human 8-Oxoguanine Glycosylase OGG1 Cleaves Abasic Sites and Covalently Conjugates to 3′-DNA Termini via Cysteine and Histidine Addition. *ChemBioChem* **2025**, *26*, No. e202400705.
(19) Mohni, K. N.; Wessel, S. R.; Zhao, R.; Wojciechowski, A. C.; Luzwick, J. W.; Layden, H.; Eichman, B. F.; Thompson, P. S.; Mehta, K. P. M.; Cortez, D. HMCES Maintains Genome Integrity by Shielding Abasic Sites in Single-Strand DNA. *Cell* **2019**, *176*, 144−153.
(20) Amidon, K. M.; Eichman, B. F. Structural biology of DNA abasic site protection by SRAP proteins. *DNA Repair* **2020**, *94*, 102903.
(21) Bellamri, M.; Terrell, J. T.; Brandt, K.; Gruppi, F.; Turesky, R. J.; Rizzo, C. J. Anthracyclines React with Apurinic/Apyrimidinic Sites in DNA. *ACS Chem. Biol.* **2023**, *18*, 1315−1323.
(22) Krapcho, A. P.; Petry, M. E.; Getahun, Z.; Landi, J. J., Jr.; Stallman, J.; Polsenberg, J. F.; Gallagher, C. E.; Maresch, M. J.; Hacker, M. P.; Giuliani, F. C.; et al. 6,9-Bis[(aminoalkyl)amino]-benzo[g]isoquinoline-5,10-diones. A novel class of chromophore-modified antitumor anthracene-9,10-diones: synthesis and antitumor evaluations. *J. Med. Chem.* **1994**, *37*, 828−837.
(23) Shenkenberg, T. D.; Von Hoff, D. D. Mitoxantrone: a new anticancer drug with significant clinical activity. *Ann. Int. Med.* **1986**, *105*, 67−81.
(24) Johnson, R. K.; Zee-Cheng, R. K.; Lee, W. W.; Acton, E. M.; Henry, D. W.; Cheng, C. C. Experimental antitumor activity of aminoanthraquinones. *Cancer Treat. Rep.* **1979**, *63*, 425−439.

(25) Hasinoff, B. B.; Wu, X.; Patel, D.; Kanagasabai, R.; Karmahapatra, S.; Yalowich, J. C. Mechanisms of action and reduced cardiotoxicity of pixantrone; a topoisomerase II targeting agent with cellular selectivity for the topoisomerase IIα isoform. *J. Pharmacol. Exp. Ther.* **2016**, *356*, 397−409.
(26) Dassault_Systèmes *Discovery Studio Visualizer, V20.1.0, 19295*; Dassault Systèmes: San Diego, CA, 2019.
(27) Dennington, R., Keith, T. A., Millam, J. M. *GaussView 6.1*, Semichem Inc., Shawnee Mission, KS, 2016
(28) Frisch, M. J.; Trucks, G. W.; Schlegel, H. B.; Scuseria, G. E.; Robb, M. A.; Cheeseman, J. R.; Scalmani, G.; Barone, V.; Petersson, G. A.; Nakatsuji, H.; Li, X.; Caricato, M.; Marenich, A. V.; Bloino, J.; Janesko, B. G.; Gomperts, R.; Mennucci, B.; Hratchian, H. P.; Ortiz, J. V.; Izmaylov, A. F.; Sonnenberg, J. L.; Williams; Ding, F.; Lipparini, F.; Egidi, F.; Goings, J.; Peng, B.; Petrone, A.; Henderson, T.; Ranasinghe, D.; Zakrzewski, V. G.; Gao, J.; Rega, N.; Zheng, G.; Liang, W.; Hada, M.; Ehara, M.; Toyota, K.; Fukuda, R.; Hasegawa, J.; Ishida, M.; Nakajima, T.; Honda, Y.; Kitao, O.; Nakai, H.; Vreven, T.; Throssell, K.; Montgomery, J. A., Jr.; Peralta, J. E.; Ogliaro, F.; Bearpark, M. J.; Heyd, J. J.; Brothers, E. N.; Kudin, K. N.; Staroverov, V. N.; Keith, T. A.; Kobayashi, R.; Normand, J.; Raghavachari, K.; Rendell, A. P.; Burant, J. C.; Iyengar, S. S.; Tomasi, J.; Cossi, M.; Millam, J. M.; Klene, M.; Adamo, C.; Cammi, R.; Ochterski, J. W.; Martin, R. L.; Morokuma, K.; Farkas, O.; Foresman, J. B.; Fox, D. J. *Gaussian 16*. Rev. C.01: Wallingford, CT, 2016.
(29) Galindo-Murillo, R.; Robertson, J. C.; Zgarbova, M.; Sponer, J.; Otyepka, M.; Jurecka, P.; Cheatham, T. E., 3rd Assessing the Current State of Amber Force Field Modifications for DNA. *J. Chem. Theory Comput.* **2016**, *12*, 4114−4127.
(30) Wang, J.; Wolf, R. M.; Caldwell, J. W.; Kollman, P. A.; Case, D. A. Development and testing of a general amber force field. *J. Comput. Chem.* **2004**, *25*, 1157−1174.
(31) Vanquelef, E.; Simon, S.; Marquant, G.; Garcia, E.; Klimerak, G.; Delepine, J. C.; Cieplak, P.; Dupradeau, F. Y. R.E.D. Server: a web service for deriving RESP and ESP charges and building force field libraries for new molecules and molecular fragments. *Nucleic Acids Res.* **2011**, *39*, W511−517.
(32) Izadi, S.; Anandakrishnan, R.; Onufriev, A. V. Building Water Models: A Different Approach. *J. Phys. Chem. Lett.* **2014**, *5*, 3863−3871.
(33) Joung, I. S.; Cheatham, T. E., 3rd Determination of alkali and halide monovalent ion parameters for use in explicitly solvated biomolecular simulations. *J. Phys. Chem. A* **2008**, *112*, 9020−9041.
(34) Case, D. A.; Aktulga, H. M.; Belfon, K.; Cerutti, D. S.; Cisneros, G. A.; Cruzeiro, V. W. D.; Forouzesh, N.; Giese, T. J.; Gotz, A. W.; Gohlke, H.; Izadi, S.; Kasavajhala, K.; Kaymak, M. C.; King, E.; Kurtzman, T.; Lee, T. S.; Li, P.; Liu, J.; Luchko, T.; Luo, R.; Manathunga, M.; Machado, M. R.; Nguyen, H. M.; O'Hearn, K. A.; Onufriev, A. V.; Pan, F.; Pantano, S.; Qi, R.; Rahnamoun, A.; Risheh, A.; Schott-Verdugo, S.; Shajan, A.; Swails, J.; Wang, J.; Wei, H.; Wu, X.; Wu, Y.; Zhang, S.; Zhao, S.; Zhu, Q.; Cheatham, T. E., 3rd; Roe, D. R.; Roitberg, A.; Simmerling, C.; York, D. M.; Nagan, M. C.; Merz, K. M., Jr. AmberTools. *J. Chem. Inf. Model.* **2023**, *63*, 6183−6191.
(35) Roe, D. R.; Brooks, B. R. A protocol for preparing explicitly solvated systems for stable molecular dynamics simulations. *J. Chem. Phys.* **2020**, *153*, 054123.
(36) Le Grand, S.; Götz, A. W.; Walker, R. C. SPFP: Speed without compromise—A mixed precision model for GPU accelerated molecular dynamics simulations. *Comput. Phys. Commun.* **2013**, *184*, 374−380.
(37) Roe, D. R.; Cheatham, T. E., 3rd PTRAJ and CPPTRAJ: Software for Processing and Analysis of Molecular Dynamics Trajectory Data. *J. Chem. Theory Comput.* **2013**, *9*, 3084−3095.
(38) Roe, D. R.; Cheatham, T. E., 3rd Parallelization of CPPTRAJ enables large scale analysis of molecular dynamics trajectory data. *J. Comput. Chem.* **2018**, *39*, 2110−2117.
(39) Rosa, S.; Fortini, P.; Karran, P.; Bignami, M.; Dogliotti, E. Processing in vitro of an abasic site reacted with methoxyamine: a new assay for the detection of abasic sites formed in vivo. *Nucleic Acids Res.* **1991**, *19*, 5569−5574.
(40) Aue, W. P.; Bartholdi, E.; Ernst, R. R. Two-dimensional spectroscopy. Application to nuclear magnetic resonance. *J. Chem. Phys.* **1976**, *64*, 2229−2246.
(41) Jeener, J.; Meier, B. H.; Bachmann, P.; Ernst, R. R. Investigation of exchange processes by two-dimensional NMR spectroscopy. *J. Chem. Phys.* **1979**, *71*, 4546−4553.
(42) Wagner, R.; Berger, S. Gradient-Selected NOESY-A Fourfold Reduction of the Measurement Time for the NOESY Experiment. *J. Magn. Reson.* **1996**, *123*, 119−121.
(43) Lee, W.; Tonelli, M.; Markley, J. L. NMRFAM-SPARKY: enhanced software for biomolecular NMR spectroscopy. *Bioinformatics* **2015**, *31*, 1325−1327.
(44) Keepers, J. W.; James, T. L. A theoretical study of distance determinations from NMR. Two-dimensional nuclear overhauser effect spectra. *J. Magn. Reson.* **1984**, *57*, 404−426.
(45) Borgias, B. A.; James, T. L. Two-dimensional nuclear Overhauser effect: complete relaxation matrix analysis. *Methods Enzymol.* **1989**, *176*, 169−183.
(46) James, T. L. Relaxation matrix analysis of two-dimensional nuclear Overhauser effect spectra. *Curr. Opin. Struct. Biol.* **1991**, *1*, 1042−1053.
(47) Borgias, B. A.; James, T. L. MARDIGRAS-A procedure for matrix analysis of relaxation for discerning geometry of an aqueous structure. *J. Magn. Reson.* **1990**, *87*, 475−487.
(48) Arnott, S.; Hukins, D. W. L. Optimised parameters for A-DNA and B-DNA. *Biochem. Biophys. Res. Commun.* **1972**, *47*, 1504−1509.
(49) *Molecular Operating Environment (MOE) 2013.08*, Chemical Computing Group Inc., 1010 Sherbooke St. West, Suite 910, Montreal, QC, Canada, H3A 2R7, 2015
(50) Schafmeister, C. E. A.; Ross, W. S.; Romanovski, V. *XLEAP*; University of California: San Francisco, San Francisco, CA, 1995.
(51) Case, D. A.; Cheatham III, T. E.; Darden, T.; Gohlke, H.; Luo, R.; Merz, K. M., Jr.; Onufriev, A.; Simmerling, C.; Wang, B.; Woods, R. J. The Amber biomolecular simulation programs. *J. Comput. Chem.* **2005**, *26*, 1668−1688.
(52) Case, D. A.; Aktulga, H. M.; Belfon, K.; Ben-Shalom, I. Y.; Berryman, J. T.; Brozell, S. R.; Carvahol, F. S.; Cerutti, D. S.; Cheatham, I. T. E.; Cisneros, G. A.; Cruzeiro, V. W. D.; Darden, T. A.; Forouzesh, N.; Ghazimirsaeed, M.; Giambaşu, G.; Giese, T.; Gilson, M. K.; Gohlke, H.; Goetz, A. W.; Harris, J.; Huang, Z.; Izadi, S.; Izmailov, S. A.; Kasavajhala, K.; Kaymak, M. C.; Kolossv\'a ry, I.; Kovalenko, A.; Kurtzman, T.; Lee, T. S.; Li, P.; Li, Z.; Lin, C.; Liu, J.; Luchko, T.; Luo, R.; Machado, M.; Manathunga, M.; Merz, K. M.; Miao, Y.; Mikhailovskii, O.; Monard, G.; Nguyen, H.; O'Hearn, K. A.; Onufriev, A.; Pan, F.; Pantano, S.; Rahnamoun, A.; Roe, D. R.; Roitberg, A.; Sagui, C.; Schott-Verdugo, S.; Shajan, A.; Shen, J.; Simmerling, C. L.; Skrynnikov, N. R.; Smith, J.; Swails, J.; Walker, R. C.; Wang, J.; Wang, J.; Wu, X.; Wu, Y.; Xiong, Y.; Xue, Y.; York, D. M.; Zhao, C.; Zhu, Q.; Kollman, P. A. *AMBER, 2025*; University of California: San Francisco, San Francisco, CA, 2025.
(53) Wang, J. M.; Cieplak, P.; Kollman, P. A. How well does a restrained electrostatic potential (RESP) model perform in calculating conformational energies of organic and biological molecules? *J. Comput. Chem.* **2000**, *21*, 1049−1074.
(54) Bashford, D.; Case, D. A. Generalized born models of macromolecular solvation effects. *Annu. Rev. Phys. Chem.* **2000**, *51*, 129−152.
(55) Pettersen, E. F.; Goddard, T. D.; Huang, C. C.; Couch, G. S.; Greenblatt, D. M.; Meng, E. C.; Ferrin, T. E. UCSF Chimera–a visualization system for exploratory research and analysis. *J. Comput. Chem.* **2004**, *25*, 1605−1612.
(56) Jancarik, J.; Kim, S. H. Sparse matrix sampling: a screening method for crystallization of proteins. *J. Appl. Crystallogr.* **1991**, *24*, 409−411.
(57) Wagner, R.; Berger, S. Gradient-selected NOESY - A fourfold reduction of the measurement time for the NOESY experiment. *J. Magn. Res. A* **1996**, *123*, 119−121.

https://doi.org/10.1021/acs.biochem.6c00116
Biochemistry XXXX, XXX, XXX−XXX

(58) Otwinowski, Z.; Minor, W. Processing of X-ray diffraction data collected in oscillation mode. *Macromol. Crystallogr.* **1997**, *276*, 307−326.
(59) Terwilliger, T. C.; Adams, P. D.; Read, R. J.; McCoy, A. J.; Moriarty, N. W.; Grosse-Kunstleve, R. W.; Afonine, P. V.; Zwart, P. H.; Hung, L. W. Decision-making in structure solution using Bayesian estimates of map quality: The PHENIX AutoSol wizard. *Acta Crystallogr. D Biol. Crystallogr.* **2009**, *65*, 582−601.
(60) Adams, P. D.; Afonine, P. V.; Bunkoczi, G.; Chen, V. B.; Davis, I. W.; Echols, N.; Headd, J. J.; Hung, L. W.; Kapral, G. J.; Grosse-Kunstleve, R. W.; McCoy, A. J.; Moriarty, N. W.; Oeffner, R.; Read, R. J.; Richardson, D. C.; Richardson, J. S.; Terwilliger, T. C.; Zwart, P. H. PHENIX: A comprehensive Python-based system for macromolecular structure solution. *Acta Crystallogr. D Biol. Crystallogr.* **2010**, *66*, 213−221.
(61) Liebschner, D.; Afonine, P. V.; Baker, M. L.; Bunkoczi, G.; Chen, V. B.; Croll, T. I.; Hintze, B.; Hung, L.-W.; Jain, S.; McCoy, A. J.; Moriarty, N. W.; Oeffner, R. D.; Poon, B. K.; Prisant, M. G.; Read, R. J.; Richardson, J. S.; Richardson, D. C.; Sammito, M. D.; Sobolev, O. V.; Stockwell, D. H.; Terwilliger, T. C.; Urzhumtsev, A. G.; Videau, L. L.; Williams, C. J.; Adams, P. D. Macromolecular structure determination using X-rays, neutrons and electrons: Recent developments in Phenix. *Acta Crystallogr. D Struct. Biol.* **2019**, *75*, 861−877.
(62) Emsley, P.; Cowtan, K. Coot: model-building tools for molecular graphics. *Acta Crystallogr. Sect. A:Fundam. Crystallogr.* **2004**, *60*, 2126−2132.
(63) Murshudov, G. N.; Skubák, P.; Lebedev, A. A.; Pannu, N. S.; Steiner, R. A.; Nicholls, R. A.; Winn, M. D.; Long, F.; Vagin, A. A. REFMAC5 for the refinement of macromolecular crystal structures. *Acta Crystallogr. D Biol. Crystallogr.* **2011**, *67*, 355−367.
(64) Brunger, A. T. Free R value: A novel statistical quantity for assessing the accuracy of crystal structures. *Nature* **1992**, *355*, 472−475.
(65) Schuttelkopf, A. W.; van Aalten, D. M. F. PRODRG: a tool for high-throughput crystallography of protein-ligand complexes. *Acta Crystallogr. D* **2004**, *60*, 1355−1363.
(66) Reid, B. R. Sequence-specific assignments and their use in NMR studies of DNA structure. *Q. Rev. Biophys.* **1987**, *20*, 1−34.
(67) Patel, D. J.; Shapiro, L.; Hare, D. DNA and RNA: NMR studies of conformations and dynamics in solution. *Q. Rev. Biophys.* **1987**, *20*, 35−112.
(68) Boelens, R.; Scheek, R. M.; Dijkstra, K.; Kaptein, R. Sequential assignment of imino- and amino-proton resonances in ^{1}H NMR spectra of oligonucleotides by two-dimensional NMR spectroscopy. Application to a *lac* operator fragment. *J. Magn. Reson.* **1985**, *62*, 378−386.
(69) Krapcho, A. P.; Landi, J. J., Jr.; Hacker, M. P.; McCormack, J. J. Synthesis and antineoplastic evaluations of 5,8-bis[(aminoalkyl)-amino]-1-azaanthracene-9,10-diones. *J. Med. Chem.* **1985**, *28*, 1124−1126.
(70) Hazlehurst, L. A.; Krapcho, A. P.; Hacker, M. P. Correlation of DNA reactivity and cytotoxicity of a new class of anticancer agents: aza-anthracenediones. *Cancer Lett.* **1995**, *91*, 115−124.
(71) Hazlehurst, L. A.; Krapcho, A. P.; Hacker, M. P. Comparison of aza-anthracenedione-induced DNA damage and cytotoxicity in experimental tumor cells. *Biochem. Pharmacol.* **1995**, *50*, 1087−1094.
(72) Péan, E.; Flores, B.; Hudson, I.; Sjoberg, J.; Dunder, K.; Salmonson, T.; Gisselbrecht, C.; Laane, E.; Pignatti, F. The European Medicines Agency Review of Pixantrone for the Treatment of Adult Patients With Multiply Relapsed or Refractory Aggressive Non-Hodgkin's B-Cell Lymphomas: Summary of the Scientific Assessment of the Committee for Medicinal Products for Human Use. *Oncologist* **2013**, *18*, 625−633.
(73) Pettengell, R.; Kaur, J. Pixantrone dimaleate for treating non-Hodgkin's lymphoma. *Expert Opin. Orphan D* **2015**, *3*, 747−757.
(74) Cavalletti, E.; Crippa, L.; Mainardi, P.; Oggioni, N.; Cavagnoli, R.; Bellini, O.; Sala, F. Pixantrone (BBR 2778) has reduced cardiotoxic potential in mice pretreated with doxorubicin: comparative studies against doxorubicin and mitoxantrone. *Invest. New Drugs* **2007**, *25*, 187−195.
(75) Hacker, M.; McKennon, M.; Singer, J. W. Lack of iron binding by pixantrone is associated with reduced production of reactive oxygen species and myoctye cytotoxicity in vitro. *Blood* **2009**, *114*, 4806.
(76) Halliwell, B., Gutteridge, J. M. *Free Radicals in Biology and Medicine*, 5th ed.; Oxford University Press, 2015
(77) Gao, Y. G.; Liaw, Y. C.; Li, Y. K.; van der Marel, G. A.; van Boom, J. H.; Wang, A. H. Facile formation of a crosslinked adduct between DNA and the daunorubicin derivative MAR70 mediated by formaldehyde: molecular structure of the MAR70-d(CGTnACG) covalent adduct. *Proc. Natl. Acad. Sci. U.S.A.* **1991**, *88*, 4845−4849.
(78) Wang, A. H.; Gao, Y. G.; Liaw, Y. C.; Li, Y. K. Formaldehyde cross-links daunorubicin and DNA efficiently: HPLC and X-ray diffraction studies. *Biochemistry* **1991**, *30*, 3812−3815.
(79) Konda, S. K.; Wang, H.; Cutts, S. M.; Phillips, D. R.; Collins, J. G. Binding of pixantrone to DNA at CpA dinucleotide sequences and bulge structures. *Org. Biomol. Chem.* **2015**, *13*, 5972−5982.
(80) Cutts, S. M.; Nudelman, A.; Rephaeli, A.; Phillips, D. R. The power and potential of doxorubicin-DNA adducts. *IUBMB Life* **2005**, *57*, 73−81.
(81) Evison, B. J.; Mansour, O. C.; Menta, E.; Phillips, D. R.; Cutts, S. M. Pixantrone can be activated by formaldehyde to generate a potent DNA adduct forming agent. *Nucleic Acids Res.* **2007**, *35*, 3581−3589.
(82) Sczepanski, J. T.; Jacobs, A. C.; Greenberg, M. M. Self-promoted DNA interstrand cross-link formation by an abasic site. *J. Am. Chem. Soc.* **2008**, *130*, 9646−9647.
(83) Sczepanski, J. T.; Jacobs, A. C.; Majumdar, A.; Greenberg, M. M. Scope and mechanism of interstrand cross-link formation by the C4'-oxidized abasic site. *J. Am. Chem. Soc.* **2009**, *131*, 11132−11139.
(84) Sczepanski, J. T.; Hiemstra, C. N.; Greenberg, M. M. Probing DNA interstrand cross-link formation by an oxidized abasic site using nonnative nucleotides. *Bioorg. Med. Chem. Lett.* **2011**, *19*, 5788−5793.
(85) Johnson, K. M.; Price, N. E.; Wang, J.; Fekry, M. I.; Dutta, S.; Seiner, D. R.; Wang, Y.; Gates, K. S. On the formation and properties of interstrand DNA-DNA cross-links forged by reaction of an abasic site with the opposing guanine residue of 5′-CAp sequences in duplex DNA. *J. Am. Chem. Soc.* **2013**, *135*, 1015−1025.
(86) Price, N. E.; Johnson, K. M.; Wang, J.; Fekry, M. I.; Wang, Y.; Gates, K. S. Interstrand DNA-DNA cross-link formation between adenine residues and abasic sites in duplex DNA. *J. Am. Chem. Soc.* **2014**, *136*, 3483−3490.
(87) Gamboa Varela, J.; Gates, K. S. A simple, high-yield synthesis of DNA duplexes containing a covalent, thermally cleavable interstrand cross-link at a defined location. *Angew. Chem.* **2015**, *127*, 7776.
(88) Gamboa Varela, J.; Gates, K. S. Simple, high-yield syntheses of DNA duplexes containing interstrand DNA-DNA cross-links between an N^4-aminocytidine residue and an abasic site. *Curr. Protocol. Nucleic Acid Chem.* **2016**, *65*, 51611−151615.
(89) Nejad, M. I.; Guo, X.; Housh, K.; Nel, C.; Yang, Z.; Price, N. E.; Wang, Y.; Gates, K. S. Preparation and purification of oligodeoxynucleotide duplexes containing a site-specific, reduced, chemically stable covalent interstrand cross-link between a guanine residue and an abasic site. *Methods Mol. Biol.* **2019**, *1973*, 163−175.
(90) Nejad, M. I.; Price, N. E.; Haldar, T.; Lewis, C.; Wang, Y.; Gates, K. S. Interstrand DNA cross-links derived from reaction of a 2-aminopurine residue with an abasic site. *ACS Chem. Biol.* **2019**, *14*, 1481−1489.
(91) Fujiwara, A.; Hoshino, T.; Westley, J. W. Anthracycline Antibiotics. *Crit. Rev. Biotechnol.* **1985**, *3*, 133−157.
(92) McGowan, J. V.; Chung, R.; Maulik, A.; Piotrowska, I.; Walker, J. M.; Yellon, D. M. Anthracycline Chemotherapy and Cardiotoxicity. *Cardiovasc. Drugs Ther.* **2017**, *31*, 63−75.
(93) Marinello, J.; Delcuratolo, M.; Capranico, G. Anthracyclines as Topoisomerase II Poisons: From Early Studies to New Perspectives. *Int. J. Mol. Sci.* **2018**, *19*, 3480.

(94) Gewirtz, D. A. A critical evaluation of the mechanisms of action proposed for the antitumor effects of the anthracycline antibiotics adriamycin and daunorubicin. *Biochem. Pharmacol.* **1999**, *57*, 727−741.
(95) Rigacci, L.; Annibali, O.; Kovalchuk, S.; Bonifacio, E.; Pregnolato, F.; Angrilli, F.; Vitolo, U.; Pozzi, S.; Broggi, S.; Luminari, S.; Merli, F.; Spina, M.; Bolis, S.; Margiotta-Casaluci, G.; Scalzulli, R.; Cox, C.; Mamusa, A. M.; Santoro, A.; Zinzani, P. L.; Ferrari, S.; Gini, G.; Vigliotti, M. L.; Mule, A.; Flenghi, L.; Fondazione Italiana, L. Nonpeghylated liposomal doxorubicin combination regimen (R-COMP) for the treatment of lymphoma patients with advanced age or cardiac comorbidity. *Hematol. Oncol.* **2020**, *38*, 478−486.
(96) Lagerlöf, I.; Fohlin, H.; Enblad, G.; Glimelius, B.; Goldkuhl, C.; Palma, M.; Åkesson, L.; Glimelius, I.; Molin, D. Limited, But Not Eliminated, Excess Long-Term Morbidity in Stage I-IIA Hodgkin Lymphoma Treated With Doxorubicin, Bleomycin, Vinblastine, and Dacarbazine and Limited-Field Radiotherapy. *J. Clin. Oncol.* **2022**, *40*, 1487−1496.
(97) Herman, E. H.; Zhang, J.; Hasinoff, B. B.; Clark, J. R., Jr.; Ferrans, V. J. Comparison of the structural changes induced by doxorubicin and mitoxantrone in the heart, kidney and intestine and characterization of the Fe(III)-mitoxantrone complex. *J. Mol. Cell. Cardiol.* **1997**, *29*, 2415−2430.
(98) Tokarska-Schlattner, M.; Wallimann, T.; Schlattner, U. Alterations in myocardial energy metabolism induced by the anti-cancer drug doxorubicin. *C. R. Biol.* **2006**, *329*, 657−668.
(99) Tokarska-Schlattner, M.; Zaugg, M.; Zuppinger, C.; Wallimann, T.; Schlattner, U. New insights into doxorubicin-induced cardiotoxicity: the critical role of cellular energetics. *J. Mol. Cell. Cardiol.* **2006**, *41*, 389−405.
(100) Doroshow, J. H.; Esworthy, R. S.; Chu, F. F. Control of doxorubicin-induced, reactive oxygen-related apoptosis by glutathione peroxidase 1 in cardiac fibroblasts. *Biochem. Biophys. Rep.* **2020**, *21*, 100709.
(101) Minko, I. G.; Moellmer, S. A.; Luzadder, M. M.; Tomar, R.; Stone, M. P.; McCullough, A. K.; Stephen Lloyd, R. Interaction of mitoxantrone with abasic sites - DNA strand cleavage and inhibition of apurinic/apyrimidinic endonuclease 1, APE1. *DNA Repair* **2024**, *133*, 103606.

https://doi.org/10.1021/acs.biochem.6c00116
Biochemistry XXXX, XXX, XXX−XXX

Characterization of Regioisomeric Conjugates Arising from Pixantrone at AP Sites in DNA

Yizhi Fu[1], John T. Terrell[1], Andrew H. Kellum Jr.[1], Pradeep S. Pallan[2], Rodrigo Galindo-Murillo[3], Carmelo J. Rizzo[1], Martin Egli[2,4,5] and Michael P. Stone[1,4,5,*]

Supporting Information

[1]Department of Chemistry, Vanderbilt University, Nashville, TN 37235, USA
[2]Department of Biochemistry, Vanderbilt University, School of Medicine, Nashville, TN 37232, USA
[3]Ionis Pharmaceuticals Inc., Carlsbad, CA 92010, USA
[4]Center for Structural Biology, Vanderbilt University, Nashville, TN 37235, USA,
[5]Vanderbilt-Ingram Cancer Center, Vanderbilt University Medical Center, Nashville, TN 37232, USA

*To whom correspondence should be addressed:

Michael P. Stone
615-322-2589
michael.p.stone@vanderbilt.edu

Table of Contents

Results and Discussion

X-ray Crystallography. The crystal structure of the modified Dickerson-Drew Dodecamer (DDD) 5′ -d($C^1G^2C^3X^4A^5A^6T^7T^8C^9G^{10}C^{11}G^{12}$)-3′ with a PIX-AP conjugate (X^4) in place of G was determined by Br-SAD and refined to a resolution of 2.5 Å (**Figure S5**). The structure in the hexagonal space group $P6_422$ revealed two independent 12-mer strands, four ethylene glycol molecules and 25 waters. Residues in both strands are numbered 1 to 12 and are colored in yellow (strand A) and green (strand B) in **Figure S6**. Nucleotides A^5 to G^{12} of both strands were part of an infinite duplex with A's and T's pairing in the core and extended by symmetry-related 12-mers that used their $C^9G^{10}C^{11}G^{12}$ ends to pair with the $C^9G^{10}C^{11}G^{12}$ ends of the parent strands under formation of C:G stretches that flanked the central A:T pairs (**Figure S6 A,B**). Between A^5 and the PIX-AP conjugate, both yellow and green strands underwent a sharp turn and looped away from the duplex formed by shifted and overlapping $A^5A^6T^7T^8C^9G^{10}C^{11}G^{12}$ octamers. The abrupt change in strand direction left the central dodecamer duplex virtually straight but resulted in pronounced kinks into the major groove at the transitions between G-tracts and A-tracts at both ends (see the overlaps with #2y and #4g symmetry mates depicted in **Figure S6 A**). The Pix conjugate along with $C^1G^2C^3$ of both the yellow and green strands and symmetry-related $C^1G^2C^3X^4$ tetramers then formed another duplex that crossed the first one at a roughly 90° angle and connected infinite duplexes assembled from yellow and green octamer strands. As schematically shown in **Figure S6 B**, looped out green and yellow $C^1G^2C^3X^4$ strand portions were arranged in a consecutive fashion such that the green tetramer continued the stack initiated by the yellow tetramer, with complementary pieces contributed by symmetry-related strands (#1g and #1y). Symmetry mates #3g, #3y, #5y and #5g then completed the crossover to the other infinite duplex. In this fashion, the connectors between infinite duplexes were composed of alternating C:G dimer steps and stacked PIX moieties sandwiched between them (**Figure S6**).

An overlay of yellow and green dodecamers revealed that their $A^5A^6T^7T^8C^9G^{10}C^{11}G^{12}$ octamer portions adopted virtually identical conformations (**Figure S7**). With one exception residues adopted Southern (C2′-endo, C3′-exo) or Southeastern (C1′-exo) deoxyribose puckers. C^{11} of the yellow strand had an Eastern pucker (O4′-endo). Yellow and green strands kinked in different directions and the latter assumed a more extended conformation that allowed it to stack onto the 5′ -end (G^2) of the yellow strand with its pixantrone moiety (**Figure S6 A**).

In the connector duplexes, stacked PIX moieties were twisted by ca. 36° as they alternated with stacked C:G dimers (**Figure S8**). At the current resolution of the structure, it was not possible to determine the orientation of the aza-anthracene-9,10-dione nitrogen. Thus, the position of that nitrogen

in the PIX moiety colored in green roughly below O2 of the cytosine colored in pink in **Figure S8** is arbitrary. As well, the position of the aza-anthracene-9,10-dione nitrogen in the PIX moiety colored in pink roughly above N4 of the cytosine colored in green in **Figure S8** is arbitrary. These two PIX moieties are not symmetry-related but belong to a green DDD strand and a symmetry mate of a yellow DDD strand (pink PIX). Neither the outer ring of the PIX moiety from one DDD nor that of the pairing DDD is positioned in the vicinity of an H-bond donor or acceptor. The absence of a direct or water-mediated interaction between DNA and PIX ring did not allow us to firmly establish which one of the two atoms forming the outer bond is nitrogen and which one is carbon.

As is evident from **Figures S7 B** and **S8**, symmetry-related yellow and green DDD strand portions that established a rung between infinite duplexes were 5′ - 3′ end-to-end stacked such that CG dimers formed discontinuous (interrupted by stacked PIX moieties) major and minor grooves. In other words, O6 of G and N4 of C were directed into the pseudo major groove and N2 of G and O2 of C were directed into the pseudo minor groove along the entire stretch. Conversely, conjugated stacked pixantrones were flipped relative to one another, such that the aminoethyl moiety of one (green) sat in the minor groove and that of the other (pink) sat in the major groove (**Figure S8**). The extrahelical orientation of pixantrone in the crystal structure and the observed arrangement of two pixantrones sandwiched by C:G pairs that served to maximize stacking strongly suggested that PIX-AP conjugate formation did not require the drug to be intercalated into DNA.

Table S1. Chemical shifts (ppm) of non-exchangeable DNA protons. N.A. = not applicable; n.o. = not observed; o. = overlapped.

Nucleotide	H6/H8	H5/CH_3	H1'	H2'	H2''	H3'
C^1	7.62	5.92	5.56	1.80	2.28	4.66
A^2	8.23	N.A.	5.84	2.75	2.83	5.01
G^3	7.72	N.A.	5.54	2.60	2.70	4.39
A^4	8.08	N.A.	6.21	2.65	2.88	4.31
C^5a	7.18	5.06	5.78	1.88	2.48	4.71
C^5b	7.17	5.04	5.78	1.87	2.47	4.70
T^6a	7.58	1.49	6.24	2.50	n.o.	n.o.
T^6b	7.56	1.45	6.24	2.50	n.o	n.o
X^7	N.A.	N.A.	N.A.	N.A.	N.A.	N.A.
A^8a	8.42	N.A.	5.94	2.79	2.90	5.02
A^8b	8.41	N.A.	5.93	2.78	2.89	5.01
G^9	7.74	N.A.	5.55	2.63	2.70	4.40
A^{10}	8.10	N.A.	6.21	2.62	2.86	5.02
C^{11}	7.33	5.27	5.94	2.09	2.41	4.75
T^{12}	7.50	1.67	6.22	2.25	2.25	4.54
A^{13}	8.04	N.A.	5.96	2.54	2.66	4.82
G^{14}	7.86	N.A.	5.92	2.66	2.79	4.40
T^{15}	7.25	1.29	6.03	2.19	2.48	4.27
C^{16}	7.45	5.41	5.92	1.93	2.40	4.69
T^{17}a	7.04	0.90	5.93	2.15	2.40	4.26
T^{17}b	7.60	0.90	5.95	2.07	2.36	n.o.
C^{18}a	8.08	6.21	6.62	2.37	2.63	4.42
C^{18}b	8.07	6.20	6.52	2.35	2.54	n.o.
A^{19}a	8.18	N.A.	5.73	2.44	2.71	4.43
A^{19}b	8.16	N.A.	5.70	2.38	2.64	4.39

$G^{20}a$	7.62	N.A.	5.80	2.48	2.70	4.35
$G^{20}b$	7.61	N.A.	5.78	2.46	n.o.	n.o.
T^{21}	7.21	1.23	6.04	2.17	2.51	4.24
C^{22}	7.59	5.58	6.00	2.09	2.48	4.80
T^{23}	7.34	1.73	5.80	1.95	2.35	n.o.
G^{24}	7.94	N.A.	6.17	2.37	2.65	n.o.

Table S2. Chemical shifts (ppm) of exchangeable DNA protons. N.A. = not applicable; n.o. = not observed; o. = overlapped.

Nucleotide	N1H/N3H	N^4H_a	N^4H_b
C^1	N.A.	N.A.	N.A.
A^2	N.A.	N.A.	N.A.
G^3	12.57	N.A.	N.A.
A^4	N.A.	N.A.	N.A.
C^5	N.A.	n.o.	n.o.
T^6a	13.24	N.A.	N.A.
T^6b	13.50	N.A.	N.A.
X^7	N.A.	N.A.	N.A.
A^8	N.A.	N.A.	N.A.
G^9	12.	N.A.	N.A.
A^{10}	N.A.	N.A.	N.A.
C^{11}	N.A.	7.34	8.21
T^{12}	n.o.	N.A.	N.A.
A^{13}	N.A.	N.A.	N.A.
G^{14}	12.74	N.A.	N.A.
T^{15}	13.55	N.A.	N.A.
C^{16}	N.A.	5.78	7.89
T^{17}a	13.52	N.A.	N.A.
T^{17}b	13.45	N.A.	N.A
C^{18}	N.A.	n.o.	n.o.
A^{19}	N.A.	N.A.	N.A.
G^{20}	12.76	N.A.	N.A.
T^{21}	13.65	N.A.	N.A.
C^{22}	N.A.	6.45	8.64
T^{23}	14.15	N.A.	N.A.
G^{24}	n.o.	N.A.	N.A.

Table S3. NOE distance restraints of PIXa-AP conjugate (R_a) DNA duplex used for rMD calculations in AMBER.

Nucleotide 1	Proton	Nucleotide 2	Proton	Lower (Å)	Upper (Å)	Window (Å)
H6	1	H1'	1	2.62	3.815	0.598
H3'	1	H6	1	3.112	4.621	0.754
H2'	1	H1'	1	2.26	3.72	0.73
H2'	1	H6	1	1.862	2.122	0.13
H2'	1	H5	1	2.901	4.154	0.626
H2"	1	H1'	1	1.867	2.136	0.134
H2"	1	H6	1	1.834	3.946	1.036
H8	2	H1'	1	3.449	5.427	0.969
H8	2	H3'	1	3.495	4.116	0.311
H8	2	H2'	1	2.495	3.33	0.417
H8	2	H2"	1	2.276	2.761	0.242
H8	2	H1'	2	3.083	4.391	0.654
H3'	2	H8	2	3.97	5.485	0.577
H2'	2	H8	2	1.877	3.285	0.704
H2"	2	H1'	2	2.046	2.491	0.223
H2"	2	H8	2	1.652	2.969	0.659
H8	3	H1'	2	2.69	3.479	0.395
H8	3	H3'	2	2.486	2.912	0.213
H8	3	H2'	2	2.65	3.623	0.486
H8	3	H2"	2	2.358	3.242	0.442
H8	3	H1'	3	2.452	3.307	0.427
H3'	3	H8	3	3.808	5.081	0.416
H2'	3	H8	3	1.876	2.174	0.149
H2"	3	H8	3	1.927	2.459	0.266
H8	4	H1'	3	2.281	2.719	0.219
H8	4	H2"	3	2.054	2.417	0.182
H8	4	H1'	4	2.15	2.733	0.292
H2"	4	H8	4	1.836	2.274	0.219

H6	5	H1'	4	2.519	3.602	0.542
H6	5	H3'	4	3.242	4.493	0.626
H6	5	H2'	4	2.478	3.249	0.386
H6	5	H2"	4	2.218	2.777	0.279
H6	5	H1'	5	3.285	4.39	0.553
H5	5	H8	4	2.663	3.34	0.338
H3'	5	H6	5	3.229	4.504	0.638
H2'	5	H1'	5	2.528	3.148	0.31
H2'	5	H6	5	2.348	3.602	0.627
H2"	5	H6	5	1.875	2.81	0.467
H6	6	H1'	5	3.481	4.312	0.415
H6	6	H3'	5	3.572	4.938	0.683
H6	6	H2'	5	2.949	3.98	0.516
H6	6	H1'	6	2.977	3.501	0.262
M7	6	H1'	4	5.515	6.873	0.679
M7	6	H1'	5	4.49	6.119	0.814
M7	6	H6	5	3.372	3.931	0.280
M7	6	H1'	6	4.831	6.051	0.610
H2'	6	H1'	6	1.762	2.464	0.351
H1	7	M7	6	3.997	4.367	0.185
H1	7	H2'	6	4.002	4.443	0.220
H3	7	M7	6	5.329	5.947	0.309
H3	7	H4	7	2.709	2.869	0.080
H8	8	H1'	8	3.311	4.523	0.606
H2'	8	H8	8	2.218	2.893	0.337
H2"	8	H8	8	2.531	3.691	0.580
H8	9	H1'	8	2.842	3.148	0.153
H8	9	H3'	8	2.5	2.893	0.197
H8	9	H2"	8	2.812	3.517	0.352
H8	9	H1'	9	2.418	3.446	0.514
H3'	9	H8	9	4.122	6.082	0

H2'	9	H8	9	1.738	2.364	0.313
H2"	9	H8	9	1.789	2.576	0.393
H8	10	H1'	9	2.334	2.715	0.191
H8	10	H2"	9	2.068	2.405	0.168
H8	10	H1'	10	2.232	2.918	0.343
H2"	10	H8	10	1.849	2.19	0.170
H6	11	H1'	10	3.177	3.404	0.114
H6	11	H2'	10	2.375	3.117	0.371
H6	11	H2"	10	2.323	2.692	0.184
H6	11	H1'	11	2.785	3.8	0.508
H5	11	H8	10	3.151	4.365	0.607
H5	11	H2'	10	3.309	4.335	0.493
H5	11	H2"	10	2.553	2.999	0.223
H3'	11	H6	11	3.201	4.665	0.732
H2'	11	H1'	11	2.021	2.617	0.298
H2'	11	H5	11	2.613	3.218	0.303
H2"	11	H6	11	2.107	3.535	0.714
H2"	11	H5	11	3.495	5.259	0.862
H6	12	H1'	11	3.213	3.93	0.359
H6	12	H3'	11	4.637	5.847	0.585
H6	12	H2'	11	2.483	2.955	0.236
H6	12	H2"	11	2.446	3.276	0.415
H6	12	H1'	12	2.841	3.922	0.541
M7	12	H1'	11	4.227	5.072	0.423
M7	12	H6	11	3.183	3.627	0.222
M7	12	H5	11	3.519	3.865	0.173
M7	12	H1'	12	4.673	6.285	0.806
H3'	12	H6	12	2.401	3.653	0.626
H2'	12	H6	12	1.98	2.151	0.085
H2"	12	H6	12	1.963	2.164	0.100
H8	13	H1'	13	2.356	3.001	0.322

H2'	13	H1'	13	1.911	2.342	0.216
H2'	13	H8	13	2.026	2.711	0.343
H2"	13	H8	13	2.37	3.155	0.392
H8	14	H1'	13	2.221	3.608	0.673
H8	14	H2'	13	2.537	3.683	0.553
H8	14	H2"	13	1.923	2.187	0.132
H8	14	H1'	14	2.962	4.093	0.565
H2'	14	H1'	13	1.974	2.204	0.115
H2'	14	H8	14	2.139	2.86	0.360
H2"	14	H8	14	1.846	2.796	0.475
H6	15	H1'	14	3.126	3.648	0.261
H6	15	H3'	14	5.033	6.757	0.642
H6	15	H2'	14	2.771	3.917	0.573
H6	15	H2"	14	2.52	3.125	0.302
H6	15	H1'	15	3.046	4.109	0.532
M7	15	H8	14	3.036	3.368	0.166
M7	15	H1'	15	3.924	4.646	0.361
H2'	15	H6	15	2.096	3.222	0.563
H2"	15	H6	15	1.958	2.805	0.424
H1'	16	M7	15	3.076	3.435	0.180
H6	16	H1'	15	3.097	3.698	0.300
H6	16	H2'	15	2.562	3.858	0.648
H6	16	H2"	15	2.043	2.786	0.371
H6	16	H1'	16	3.072	3.9	0.414
H5	16	H6	15	3.284	4.6	0.658
H5	16	M7	15	3.977	5.179	0.601
H5	16	H2'	15	2.764	4.189	0.713
H5	16	H2"	15	2.703	3.777	0.537
H3'	16	H6	16	3.203	4.263	0.530
H2'	16	H1'	16	3.236	5.196	0.000
H2'	16	H6	16	2.186	3.134	0.474

H2'	16	H5	16	3.167	4.366	0.599
H2"	16	H6	16	2.415	3.513	0.549
H2"	16	H5	16	3.139	4.318	0.589
H1'	17	M7	15	4.39	4.928	0.269
H6	17	H1	7	5.819	6.556	0.368
H6	17	H3	7	4.185	5.103	0.459
H6	17	H1'	16	2.898	5.086	1.094
H6	17	H3'	16	4.805	5.744	0.35
H6	17	H2"	16	1.915	2.361	0.223
H6	17	H1'	17	3.099	4.803	0.852
M7	17	H4	7	4.001	4.435	0.217
M7	17	H1	7	4.141	4.517	0.188
M7	17	H3	7	4.097	4.608	0.256
M7	17	H1'	15	4.477	5.437	0.48
M7	17	H1'	16	4.197	5.245	0.524
M7	17	H6	16	3.072	3.624	0.276
M7	17	H5	16	3.723	4.453	0.365
M7	17	H1'	17	4.187	5.279	0.546
H3'	17	H6	17	5.491	7.829	0.689
H2'	17	H3	7	3.773	5.395	0.811
H2'	17	H6	17	2.132	4.084	0.976
H2"	17	H3	7	3.377	4.085	0.354
H2"	17	H6	17	2.028	2.663	0.317
H1'	18	H3	7	5.459	6.138	0.339
H6	18	H1'	18	3.589	5.04	0.725
H5	18	H6	17	4.321	6.126	0.762
H2'	18	H1'	18	2.413	3.61	0.599
H2'	18	H6	18	1.949	2.621	0.336
H2"	18	H1'	18	2.36	3.436	0.538
H8	19	H1'	18	4.154	4.58	0.213
H8	19	H3'	18	2.858	3.304	0.223

H8	19	H2'	18	3.454	4.63	0.588
H8	19	H2"	18	3.149	4.479	0.665
H8	19	H1'	19	3.396	4.207	0.405
H3'	19	H8	19	2.869	3.531	0.331
H2'	19	H1'	19	2.488	3.717	0.614
H2'	19	H8	19	2.35	2.969	0.309
H2"	19	H1'	19	2.233	3.098	0.433
H2"	19	H8	19	2.75	3.888	0.569
H8	20	H1'	19	3.748	4.743	0.498
H8	20	H2'	19	3.049	4.157	0.454
H8	20	H2"	19	2.071	2.571	0.25
H8	20	H1'	20	3.572	4.923	0.675
H2'	20	H8	20	2.621	3.465	0.422
H2"	20	H8	20	2.133	2.8	0.333
H6	21	H1'	20	2.94	4.105	0.582
H6	21	H2'	20	1.873	2.395	0.261
H6	21	H2"	20	2.481	3.721	0.6
H6	21	H1'	21	2.913	4.248	0.667
M7	21	H8	20	3.535	4.136	0.3
M7	21	H1'	21	4.03	5.04	0.505
H2'	21	H6	21	1.969	2.621	0.326
H2"	21	H6	21	2.126	2.73	0.302
H6	22	H1'	21	3.113	4.236	0.561
H6	22	H2'	21	2.323	2.481	0.079
H6	22	H2"	21	2.23	2.463	0.117
H6	22	H1'	22	2.782	4.027	0.622
H5	22	H6	21	3.129	3.705	0.288
H5	22	M7	21	3.587	4.252	0.332
H3'	22	H6	22	5.478	6.598	0.26
H2'	22	H1'	22	2.109	3.25	0.57
H2'	22	H6	22	2.214	2.433	0.11

H2"	22	H1'	22	1.993	2.844	0.425
H2"	22	H6	22	2.217	2.51	0.146
H6	23	H1'	22	2.928	3.926	0.499
H6	23	H2"	22	2.139	3.353	0.607
H6	23	H1'	23	3.04	3.86	0.41
M7	23	H1'	21	4.982	6.693	0.856
M7	23	H1'	22	3.737	5.735	0.999
M7	23	H6	22	3.094	3.468	0.187
M7	23	H5	22	3.616	4.066	0.225
M7	23	H1'	23	3.698	4.922	0.612
H2'	23	H1'	23	2.346	3.292	0.473
H2'	23	H6	23	1.882	2.243	0.18
H2"	23	H1'	23	2.005	2.347	0.171
H2"	23	H6	23	2.159	2.861	0.351
H8	24	H1'	23	2.586	4.396	0.905
H8	24	M7	23	3.976	5.751	0.887
H8	24	H2'	23	2.136	2.627	0.246
H8	24	H2"	23	2.133	2.63	0.249
H8	24	H1'	24	2.75	4.509	0.879
H2'	24	H1'	24	1.819	2.215	0.198
H2'	24	H8	24	2.029	2.517	0.244
H2"	24	H1'	24	2.066	3.279	0.607
H2"	24	H8	24	1.954	2.13	0.088
H2"	24	H8	24	1.954	2.13	0.088

Table S4. NOE distance restraints of PIXb-AP conjugate (R_b) DNA duplex used for rMD calculations in AMBER.

Nucleotie 1	Proton	Nucleotide 2	Proton	Lower (Å)	Upper (Å)	Window (Å)
H6	1	H1'	1	2.122	2.327	0.103
H3'	1	H6	1	2.346	2.574	0.114
H2'	1	H1'	1	3.123	4.166	0.522
H2'	1	H6	1	2.364	2.517	0.076
H2'	1	H5	1	2.389	2.611	0.111
H2"	1	H1'	1	2.252	2.374	0.061
H2"	1	H6	1	3.395	5.192	0.858
H8	2	H3'	1	2.99	3.375	0.192
H8	2	H2'	1	3.704	5.057	0.677
H8	2	H2"	1	4.24	5.356	0.558
H8	2	H1'	2	2.058	2.404	0.173
H3'	2	H8	2	2.567	3.079	0.256
H2'	2	H8	2	2.086	2.336	0.125
H2"	2	H1'	2	2.154	2.376	0.111
H2"	2	H8	2	2.704	3.34	0.318
H8	3	H1'	2	2.782	3.326	0.272
H8	3	H3'	2	2.818	3.331	0.257
H8	3	H2'	2	3.23	4.045	0.408
H8	3	H2"	2	3.951	5.43	0.739
H3'	3	H8	3	2.697	2.812	0.058
H2'	3	H8	3	2.403	2.703	0.15
H2"	3	H8	3	2.368	2.586	0.109
H8	4	H2"	3	2.532	3.139	0.304
H2"	4	H8	4	2.318	2.482	0.082
H6	5	H1'	4	3.025	3.823	0.399
H6	5	H3'	4	2.732	3.025	0.147
H6	5	H2'	4	2.33	2.606	0.138
H6	5	H2"	4	2.714	4.348	0.817

H6	5	H1'	5	2.22	2.558	0.169
H3'	5	H6	5	2.543	2.756	0.107
H2'	5	H1'	5	2.128	2.295	0.083
H2'	5	H6	5	2.571	3.468	0.448
H2"	5	H6	5	2.228	2.435	0.103
H6	6	H1'	5	2.347	3.128	0.39
H6	6	H3'	5	2.402	2.831	0.214
H6	6	H2'	5	2.394	2.978	0.292
H6	6	H1'	6	3.018	3.122	0.052
M7	6	H1'	5	3.753	4.244	0.245
M7	6	H6	5	4.086	4.534	0.224
M7	6	H1'	6	4.509	5.045	0.268
H2'	6	H1'	6	2.231	2.421	0.095
H4	7	M7	6	4.092	4.416	0.162
H1	7	M7	6	6.85	7.625	0.387
H3	7	M7	6	4.954	5.468	0.257
H3	7	H4	7	3.255	3.571	0.158
H8	8	H1'	8	3.168	4.729	0.78
H2'	8	H8	8	2.142	2.38	0.119
H2"	8	H8	8	2.08	2.221	0.07
H8	9	H1'	8	3.62	4.013	0.196
H8	9	H3'	8	2.775	3.244	0.234
H8	9	H2"	8	3.523	5.111	0.794
H3'	9	H8	9	2.713	2.817	0.052
H2'	9	H8	9	2.335	2.629	0.147
H2"	9	H8	9	2.38	2.659	0.14
H8	10	H2"	9	2.397	2.807	0.205
H2"	10	H8	10	2.392	2.749	0.179
H6	11	H1'	10	3.192	3.448	0.128
H6	11	H3'	10	2.901	3.065	0.082
H6	11	H2'	10	2.188	2.492	0.152

H6	11	H2"	10	2.951	3.852	0.451
H6	11	H1'	11	3.302	4.727	0.713
H5	11	H8	10	2.234	2.56	0.163
H5	11	H2'	10	2.294	3.499	0.603
H5	11	H2"	10	2.163	2.937	0.387
H3'	11	H6	11	2.417	2.636	0.11
H2'	11	H1'	11	2.083	2.247	0.082
H2'	11	H5	11	2.444	4.051	0.803
H2"	11	H6	11	2.238	2.684	0.223
H2"	11	H5	11	2.288	4.004	0.858
H6	12	H1'	11	2.864	3.244	0.19
H6	12	H3'	11	3.734	4.085	0.175
H6	12	H2'	11	3.524	5.02	0.748
H6	12	H2"	11	3.514	4.798	0.642
H6	12	H1'	12	2.822	2.96	0.069
M7	12	H1'	11	3.327	4.247	0.46
M7	12	H6	11	4.614	6.214	0.68
M7	12	H5	11	2.69	2.977	0.143
M7	12	H1'	12	3.193	3.767	0.287
H3'	12	H6	12	2.79	2.891	0.05
H2'	12	H6	12	2.407	2.766	0.179
H2"	12	H6	12	2.502	2.821	0.16
H8	13	H1'	13	2.271	2.758	0.243
H3'	13	H8	13	2.748	3.604	0.428
H2'	13	H1'	13	2.546	3.247	0.351
H2'	13	H8	13	2.053	2.326	0.136
H2"	13	H8	13	2.153	2.469	0.158
H8	14	H1'	13	2.159	2.478	0.16
H8	14	H3'	13	3.034	3.551	0.258
H8	14	H2'	13	3.106	4.401	0.608
H8	14	H2"	13	2.479	2.875	0.198

H8	14	H1'	14	3.09	3.742	0.326
H3'	14	H8	14	2.841	3.237	0.198
H2'	14	H1'	13	2.405	2.674	0.135
H2'	14	H8	14	2.651	3.164	0.257
H2"	14	H8	14	2.287	2.533	0.123
H6	15	H1'	14	3.231	3.913	0.341
H6	15	H3'	14	3.217	3.697	0.24
H6	15	H2'	14	3.384	5.07	0.843
H6	15	H2"	14	2.426	2.975	0.274
H6	15	H1'	15	2.935	3.173	0.119
M7	15	H8	14	3.989	4.574	0.293
M7	15	H1'	15	2.464	3.042	0.289
H3'	15	H6	15	2.722	2.874	0.076
H2'	15	H6	15	2.204	2.448	0.122
H2"	15	H6	15	2.338	2.871	0.267
H1'	16	M7	15	1.769	2.121	0.176
H6	16	H1'	15	2.963	3.164	0.1
H6	16	H3'	15	3.171	3.96	0.394
H6	16	H2'	15	2.437	4.084	0.823
H6	16	H2"	15	2.252	3.4	0.574
H6	16	H1'	16	2.15	2.545	0.198
H5	16	H6	15	2.28	2.719	0.219
H5	16	M7	15	2.417	3.112	0.348
H5	16	H2'	15	2.124	3.646	0.761
H5	16	H2"	15	2.248	3.632	0.692
H3'	16	H6	16	2.323	2.549	0.113
H2'	16	H1'	16	1.965	2.873	0.454
H2'	16	H6	16	2.241	2.69	0.224
H2'	16	H5	16	2.5	3.402	0.451
H2"	16	H6	16	2.215	2.589	0.187
H2"	16	H5	16	2.62	3.715	0.547

H1'	17	H1	7	5.302	6.397	0.548
H1'	17	M7	15	3.159	3.534	0.187
H6	17	H1'	16	2.861	3.602	0.371
H6	17	H3'	16	3.436	4.763	0.663
H6	17	H2'	16	2.599	2.952	0.176
H6	17	H2"	16	2.385	2.821	0.218
H6	17	H1'	17	2.948	3.238	0.145
M7	17	H1	7	5.028	5.574	0.273
M7	17	H3	7	5.077	5.646	0.285
M7	17	H1'	15	3.025	3.531	0.253
M7	17	H1'	16	2.63	3.036	0.203
M7	17	H5	16	2.572	2.908	0.168
M7	17	H1'	17	2.671	3.163	0.246
H3'	17	H6	17	3.241	3.707	0.233
H2'	17	H1	7	3.954	5.361	0.704
H2'	17	H6	17	2.214	2.37	0.078
H2"	17	H1	7	4.084	5.206	0.561
H2"	17	H6	17	2.398	2.667	0.135
H6	18	H1'	17	4.011	5.971	0.000
H6	18	H2'	17	2.333	3.164	0.416
H6	18	H1'	18	2.651	3.694	0.521
H5	18	H6	17	4.14	5.548	0.704
H3'	18	H6	18	2.659	4.004	0.673
H2'	18	H1'	18	2.028	3.073	0.522
H2'	18	H6	18	1.865	2.169	0.152
H2"	18	H1'	18	1.844	2.336	0.246
H8	19	H1'	18	2.752	3.645	0.446
H8	19	H3'	18	1.958	2.231	0.136
H8	19	H2'	18	2.592	3.441	0.425
H8	19	H1'	19	2.147	2.704	0.279
H3'	19	H8	19	1.943	2.17	0.113

H2'	19	H1'	19	2.165	2.339	0.087
H2'	19	H8	19	2.342	3.906	0.782
H2"	19	H1'	19	2.258	2.442	0.092
H2"	19	H8	19	2.174	2.679	0.253
H8	20	H1'	19	3.022	4.513	0.746
H8	20	H3'	19	3.327	5.024	0.829
H8	20	H2"	19	1.909	2.133	0.112
H8	20	H1'	20	3.788	4.573	0.373
H3'	20	H8	20	3.507	4.803	0.648
H2'	20	H8	20	2.272	3.334	0.531
H2"	20	H8	20	1.918	2.217	0.149
H6	21	H1'	20	3.052	3.755	0.351
H6	21	H2'	20	2.378	2.685	0.153
H6	21	H2"	20	2.316	2.829	0.257
H6	21	H1'	21	3.046	3.261	0.108
M7	21	H8	20	4.153	5.609	0.728
M7	21	H1'	21	2.689	3.156	0.233
H3'	21	H6	21	2.786	2.957	0.085
H2'	21	H6	21	2.309	2.527	0.109
H2"	21	H6	21	2.618	3.589	0.485
H6	22	H1'	21	3.202	3.496	0.147
H6	22	H2'	21	2.582	3.199	0.309
H6	22	H2"	21	2.669	2.968	0.15
H6	22	H1'	22	2.139	2.403	0.132
H5	22	H6	21	3.703	4.269	0.283
H5	22	M7	21	2.173	2.689	0.258
H3'	22	H6	22	3.125	3.37	0.122
H2'	22	H1'	22	2.123	2.283	0.08
H2'	22	H6	22	2.872	3.237	0.182
H2"	22	H1'	22	2.238	3.25	0.506
H2"	22	H6	22	2.94	3.594	0.327

H6	23	H1'	22	2.516	3.274	0.379
H6	23	H2"	22	2.998	4.179	0.591
H6	23	H1'	23	2.04	2.278	0.119
M7	23	H1'	21	3.405	3.865	0.23
M7	23	H1'	22	2.681	3.154	0.237
M7	23	H6	22	4.864	6.803	0.95
M7	23	H5	22	2.553	2.949	0.198
M7	23	H1'	23	2.79	4.063	0.636
H2'	23	H1'	23	2.696	3.822	0.543
H2'	23	H6	23	2.185	2.447	0.131
H2"	23	H1'	23	2.142	2.691	0.275
H2"	23	H6	23	2.951	3.925	0.467
H8	24	H1'	23	2.139	2.387	0.124
H8	24	H2'	23	3.048	3.382	0.167
H8	24	H2"	23	2.947	4.207	0.63
H8	24	H1'	24	1.977	2.158	0.09
H2'	24	H1'	24	2.15	2.572	0.211
H2'	24	H8	24	2.446	3.749	0.572
H2"	24	H1'	24	2.292	3.673	0.67
H2"	24	H8	24	2.188	2.846	0.329
H2"	24	H8	24	2.188	2.846	0.329

Table S5. Selected crystal data, X-ray data collection and refinement parameters.

Oligonucleotide	Modified 12-mer
Data Collection	
Oligonucleotide sequence	5′-d(CGCXAATT(Br5C)GCG)-3′[a]
Space group	$P6_422$
Unit cell constants: a, b, c [Å]	95.92, 95.92, 73.12
Unit cell constants: α, β, γ [°]	90.0, 90.0, 120.0
Resolution [Å]	27.71-1.49 (1.58-1.51)[b]
No. of unique reflections	7,367
Completeness (outer shell) [%]	99.9 (100.0)
R-merge (outer shell)	0.131 (1.212)
R-pim (outer shell)	0.022 (0.198)
I/σ(I) (outer shell)	42.00 (2.00)
Redundancy	37.5 (37.9)
Refinement	
Resolution[b]	27.71-2.49 (2.56-2.49)
Number of unique reflections	6,740 (487)
R-work	0.245 (0.620)
R-free	0.262 (0.483)
No. of nucleotide-atoms	506
No. of waters/ethylene glycol	27/4
R.m.s. deviations bonds [Å]	0.010
R.m.s. deviations angles [°]	1.38
Avg. B-factor, nucleotide atoms [Å^2]	49.43[b]
Avg. B-factor, H_2O/ethylene glycol [Å^2]	77.38/36.49

PDB entry code	7U38

[a]X is PIX-AP and Br5C is 5-Bromo-2′-deoxycytidine

[b]Outermost shell in parentheses

Supporting Figures

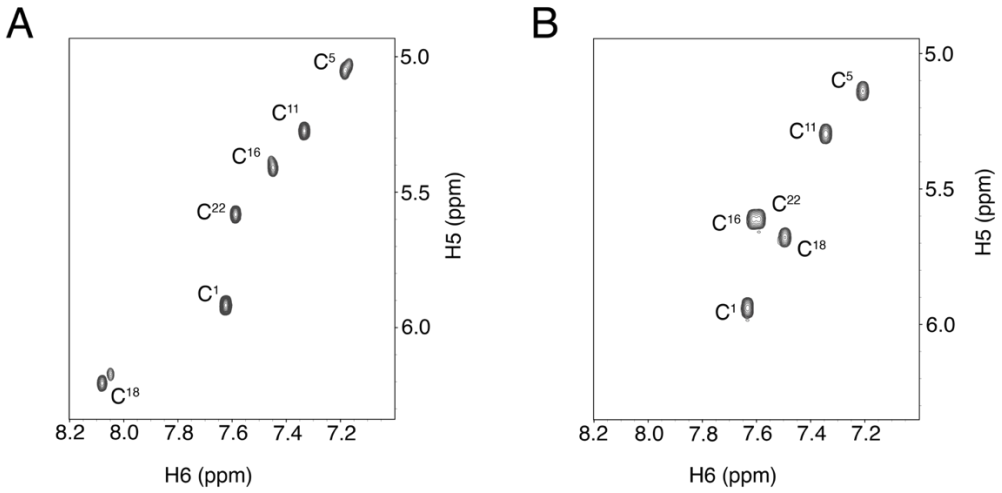

Figure S1. Two-dimensional COSY spectra of PIX-AP conjugate duplex and unmodified duplex. **A.** COSY spectrum of 5′-d($C^1A^2G^3A^4C^5T^6X^7A^8G^9A^{10}C^{11}T^{12}$)-3′:5′-d($A^{13}G^{14}T^{15}C^{16}T^{17}C^{18}A^{19}G^{20}T^{21}C^{22}T^{23}G^{24}$)-3′ (X = PIX-AP) showing scalar couplings between cytosine H5 and H6 protons. **B.** COSY spectrum of 5′-d($C^1A^2G^3A^4C^5T^6X^7A^8G^9A^{10}C^{11}T^{12}$)-3′ duplex. The spectra were acquired at 900 MHz and 288 K.

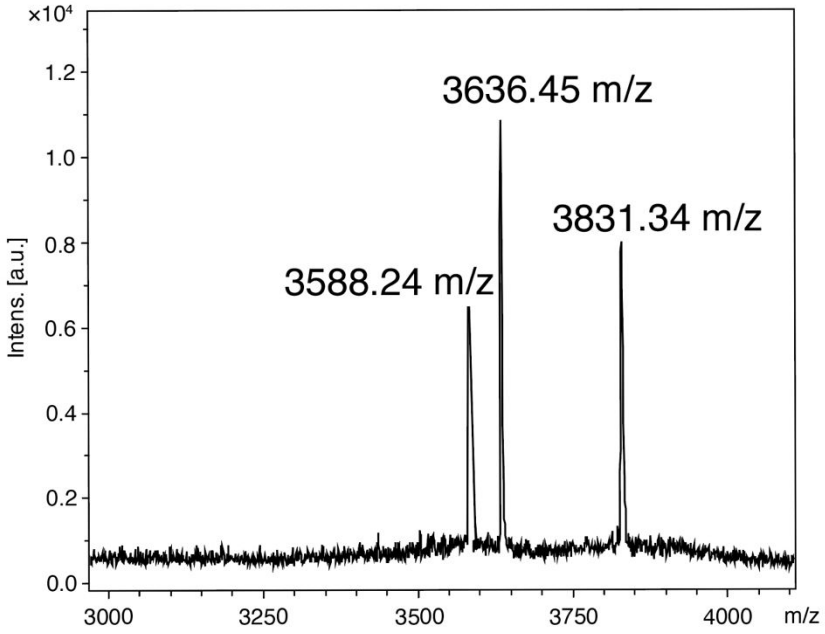

Figure S2. MALDI-TOF mass spectrum of the methoxyamine (MX)-quenched reaction. The peak at 3588.24 m/z represents the expected mass of the MX-containing strand, while the peaks at 3636.45 m/z and 3831.34 m/z represents the expected mass of the corresponding complementary strand and PIX-AP conjugate strand, respectively.

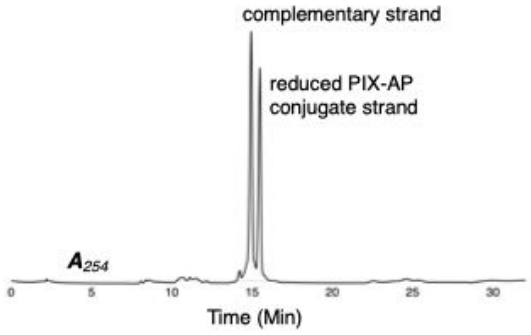

Figure S3. HPLC-UV chromatogram of the reaction of the AP-containing oligonucleotide with PIX reduced with $NaB(CN)H_3$ at 60 °C analyzed after 1 h.

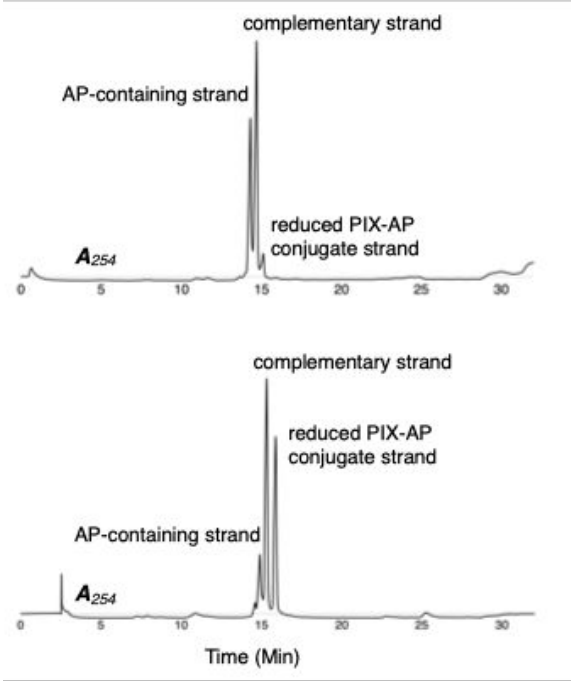

Figure S4. HPLC-UV chromatogram of the reaction of the AP-containing oligonucleotide with PIX reduced with $NaB(CN)H_3$ analyzed at 0 °C (top) and 35 °C (bottom) after 1 h.

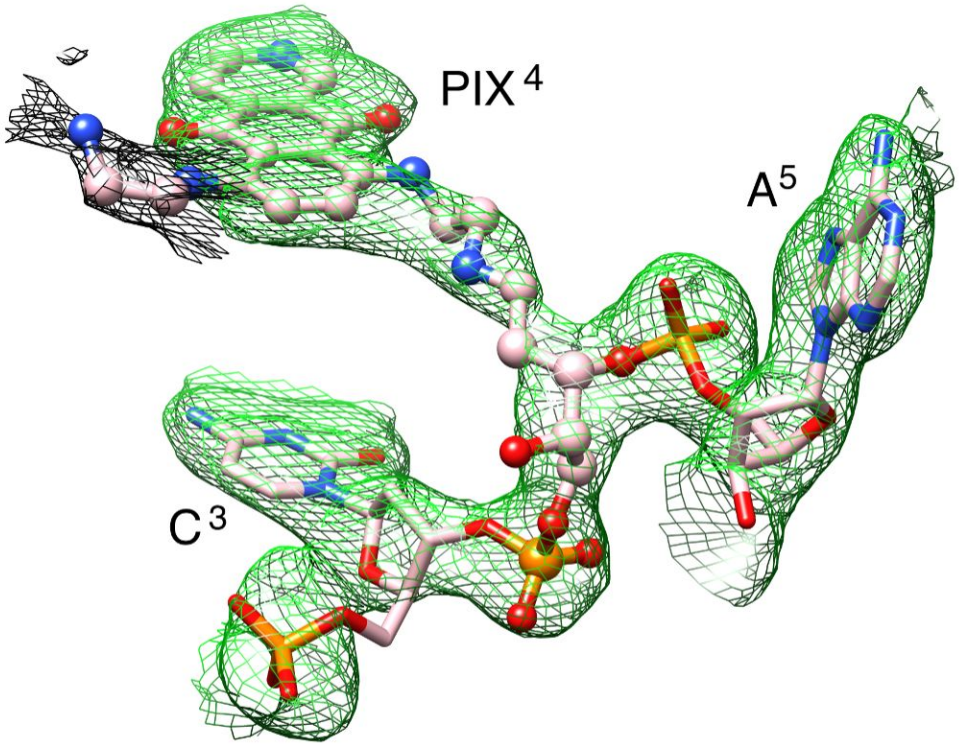

Figure S5. Final Fourier $2F_o$-F_c sum electron density (green meshwork) around the C^3-PIX-A^5 base steps drawn at ~1.1 σ threshold. The electron density around one of the diamino ethyl arms is weaker and therefore shown at ~0.8 σ threshold (grey meshwork). PIX-AP atoms are depicted in ball and stick mode. Atoms are colored salmon, red, blue and orange for carbon, oxygen, nitrogen, and phosphorus, respectively.

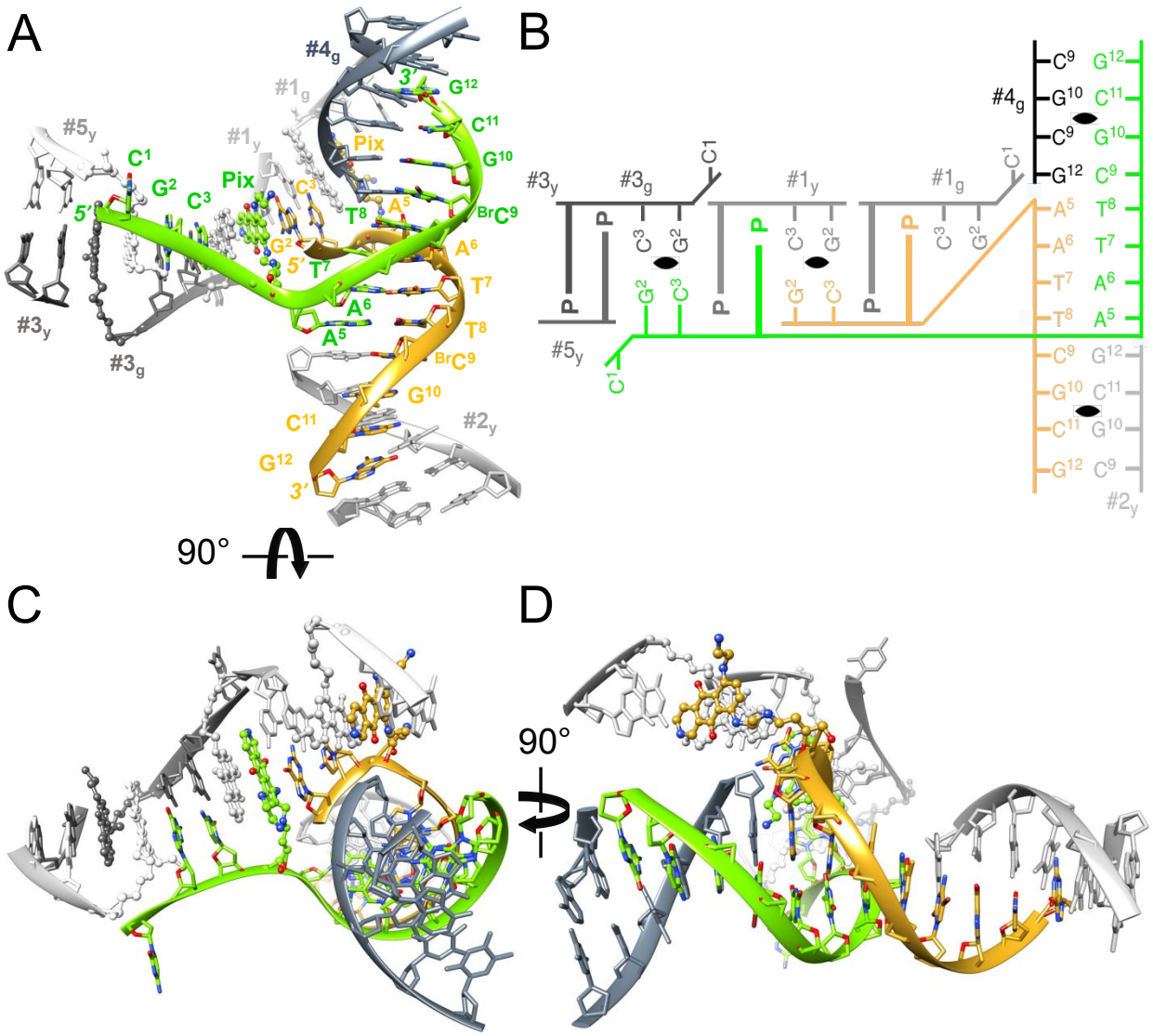

Figure S6. Lattice interactions in the crystal structure of a modified DDD with a PIX-AP conjugate. **A.** A kink in the 12-mer strands between the PIX moiety and the adjacent adenosine results in looped-out tetramers and gives rise to an infinite duplex that consists of alternating CGCG G-tracts and AATT A-tracts and roughly perpendicular crossovers that consists of alternating CG dimers and stacked PIX moieties. Symmetry-related yellow and green strands are marked #x_y and #x_g, respectively, residues of the parent yellow and green strands are labeled, and the positions of crystallographic dyads are indicated. The 5′-terminal C^1 nucleosides of yellow strands are not visible in the electron density and 5′-terminal C^1 nucleosides of green strands are extruded from the connector duplex. **B.** Schematic drawing of the lattice interactions shown in panel A with positions of crystallographic twofold rotation axes

indicated. **C.** The crossover of duplexes depicted in panel A rotated by 90° around the horizontal axis. **D.** The crossover of duplexes depicted in panel C rotated by 90° around the vertical axis.

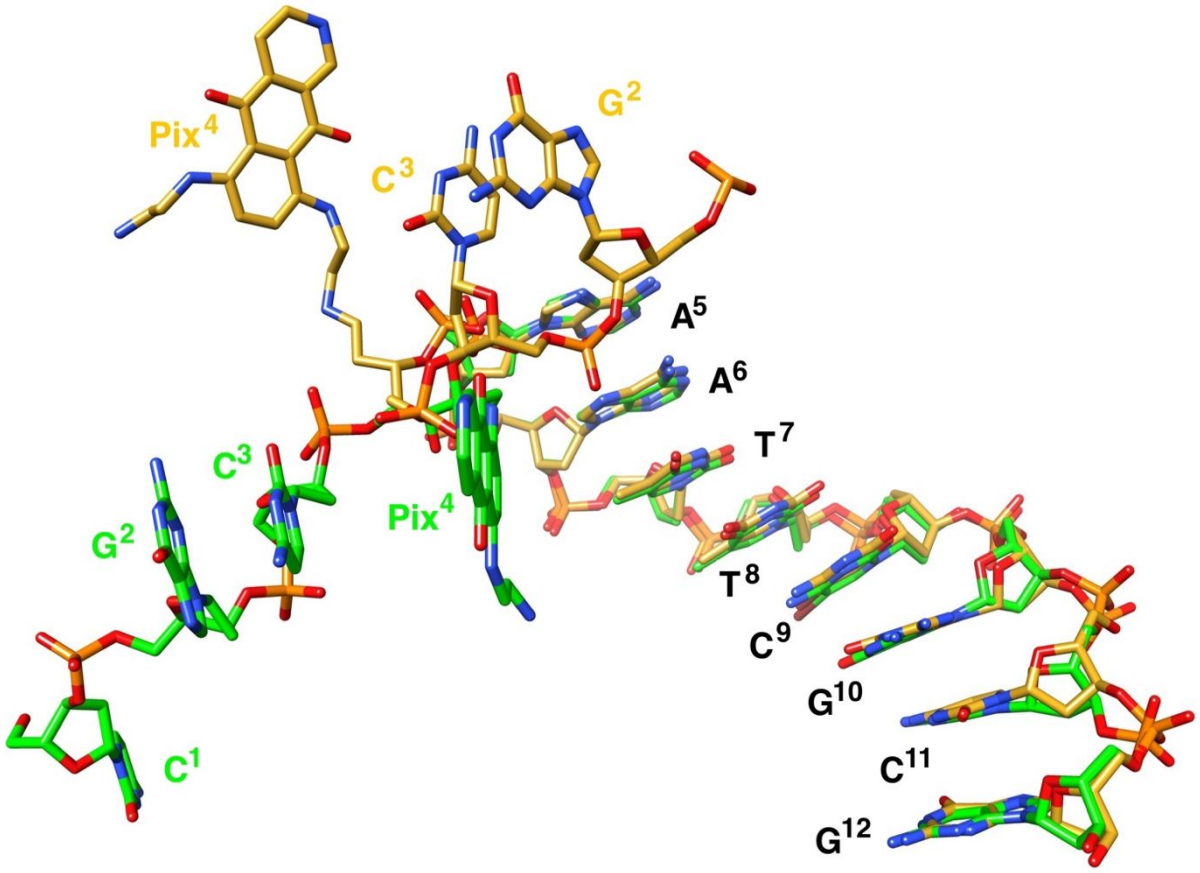

Figure S7. Superimposition of yellow and green DDD strands with PIX-AP conjugates. The resolution of the structure does not allow us to distinguish between nitrogen and carbon in the aza-anthracene-9,10-dione. As well the immediate environment of the ring in the crystal lattice is devoid of H-bond donors or acceptors that would allow a distinction between N and C-H. Hence N positions shown are arbitrarily chosen.

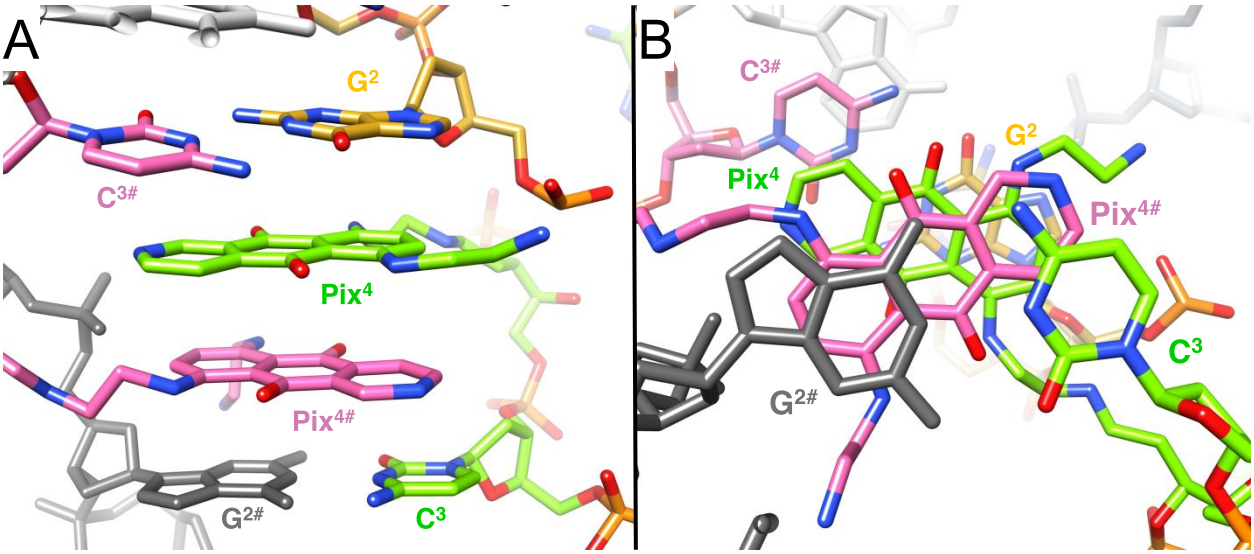

Figure S8. Stacked PIX moieties alternating with CG dimers in the connector duplex. **A.** View into the pseudo major groove. **B.** View approximately along the normal to PIX and base planes. PIX moieties and nucleotides from the parent strands (yellow and green) and contributed by symmetry mates are colored differently.